Data-Driven Adaptive Unscented Kalman Filter for Time-varying Inertia and Damping Estimation of Utility-scale IBRs Considering Current Limiter

Bendong Tan, Student Member, IEEE, Junbo Zhao, Senior Member, IEEE

Abstract—Grid-forming inverters, such as the virtual synchronous generator (VSG), can emulate constant or time-varying inertia to mitigate frequency stability issues. This paper proposes a data-driven variational Bayesian adaptive unscented Kalman filter (VBAUKF) to estimate the VSG-based inverter inertia and damping factor using its terminal measurements. By adopting the Thevenin equivalent idea, the virtual frequency of VSG is estimated first. Utilizing the estimated virtual frequency and considering the effects of the inverter current limiter, the timevarying inertia and damping factor estimation problem is reformulated into the state-space model-based dynamic state estimation framework. The measurements include the obtained virtual frequency, inverter terminal real, and reactive power while the unknowns are inverter inertia, damping factor, internal virtual rotor speed, and angle. To this end, an innovative VBAUKF is proposed with the advantages of dealing with unknown and time-varying models and measurement uncertainties. Numerical results on the modified IEEE 39-bus system and IEEE 118bus power system demonstrate that the proposed estimator significantly outperforms other state-of-the-art approaches under various scenarios.

Index Terms—Inertia estimation, virtual inertia, Variational Bayesian estimation, unscented Kalman filter, dynamic estimation, inverter-based resources, power system dynamics.

I. INTRODUCTION

THE frequency variation from the nominal level reflects the imbalance degree between the generation and consumption, while the inertia in the system is able to restrain the variation. However, with the rapid growth of inverter-based resources (IBRs), like wind and photovoltaic energies, inertia in the modern power grid has been sharply reduced [1]. This yields larger frequency deviations as well as an exorbitant rate of change of frequency (ROCOF), which could lead to underfrequency relays activation. For real-time grid operations with a high penetration of IBRs, maintaining adequate inertia and damping is essential to ensure grid reliability. Based on the values of inertia and damping factor, control actions (like changing generator outputs, adjusting control systems, or shedding load) can be taken to ensure system stability. To assist system operators in taking the appropriate precautions, it is meaningful to precisely analyze the inertia level at each node and its variation trend at each time instant [2].

This work is partially supported by US Department of Energy Advanced Grid Modeling program as well as National Science Foundation under award 2328241

B. Tan and J. Zhao are with the Department of Electrical and Computer Engineering, University of Connecticut, Storrs, CT 06269 USA (e-mail: bendong.tan@uconn.edu, junbo@uconn.edu).

By utilizing phasor measurement units (PMUs) data under large disturbance, many efforts have been made to estimate inertia constant inside synchronous generators (SG) or areas. Since inertia is mathematically represented to be the proportion of the active power deviation to ROCOF, the main issue is to calculate ROCOF after a disturbance within several seconds. This requires the time derivative of bus frequency measured with PMUs. However, noise and discontinuities in bus frequency may lead to significant numerical issues. To mitigate these effects, a fifth-order approximation with respect to time to estimate ROCOF is proposed in [3] but it requires a 20-second window to conduct curve fitting that may contain the effects of primary frequency control. This leads to inaccurate inertia estimation. By utilizing the Thevenin equivalent, [6] directly estimates rotor speed, which is further merged into the unscented Kalman filter (UKF) framework to estimate inertia. To perform regional power system inertia estimation, [7]–[9] derive the analytic relationship between inertia constant and oscillation modes. Based on the frequency divider theory, [10] builds identification models to estimate the spatial inertia distribution across the grid nodes. [11] also develops a frequency domain-based approach to identify the inertia constant of a single generator. Nevertheless, both [10] and [11] require accurate model information. To estimate regional power system inertia with ambient data, the explicit relationship between area inertia and interarea oscillation modes is confined in [13], while [14] developed an autoregressive-based method to identify area inertia. However, [13] and [14] are only applicable to areas that are oscillating against each other. Estimation methods for system inertia, applied to realistic power systems like those in the UK, Hawaiian Islands, and WECC, utilize system identification [15] and machine learning [16], [17]. These methods have been validated under actual measurement data. Nevertheless, they are limited to synchronous generator-dominated system inertia estimation.

Note that the aforementioned works are focused on synchronous generator inertia estimation, while the inertia of non-synchronous generators is rarely investigated. As some advanced inertial control schemes, such as virtual synchronous generator (VSG), are designed for IBRs to provide frequency support, how to estimate the constant or time-varying virtual inertia inside inverters becomes challenging. By linearizing the dynamic system, [18] and [19] identify the inertia constant of IBRs via using ambient measurements, but some state variables, i.e., intermediate state variables inside the phase

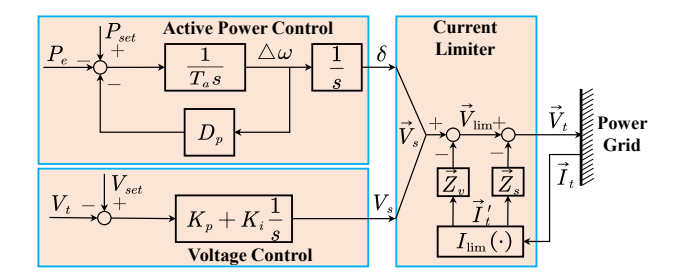


Fig. 1. VSG Control chart of IBRs with current limiter.

lock loop, are assumed to be known, which is unrealistic. Furthermore, it doesn't have the capability of estimating the time-varying virtual inertia of IBRs. To this end, [20] proposes an inertia estimation formula to estimate the constant or timevarying virtual inertia for IBRs, however, it is plagued by convergence speed. [21] mitigates the numerical issues but does not perform damping factor estimation well under timevarying inertia. Besides, a current limiter usually exists to regulate the maximum fault current for IBRs and this limiter can affect the virtual inertia support. However, none of the existing work has considered this, leading to bias in inertia estimation results.

To address these issues, a data-driven time-varying inertia estimator for IBRs considering the current limiter is developed in the paper. The contributions are summarized below:

- A time-varying inertia and damping factor estimation framework considering the current limiter of IBRs has been developed by deriving the proper state-space model. This allows us to mitigate the effects of the current limiter of IBRs. This is the first time to address that in the literature.
- This paper proposes the variational Bayesian adaptive unscented Kalman filter (VBAUKF), a novel approach for inferring the unknown posterior distributions of model and measurement noise through Bayesian approximation. Additionally, the measurement noise covariance matrix is dynamically adapted, employing strategies such as exponentially discarding outdated information when the current limiter is inactive, and gradually modifying the measurement noise covariance matrix upon the activation of the current limiter. As a result, the discontinuity effects caused by the current limiter can be mitigated. This leads to significantly improved inertia and damping factor tracking speed and accuracy while being robust to unknown noise and the effects of the current limiter.
- The proposed method is data-driven and only requires the IBR terminal PMU or other similar measurements (e.g., synchronized wave measurements) of IBRs. It is able to estimate constant and time-varying inertia as well as damping parameters. Note that the damping parameter is difficult to track for [20] and [21] in the presence of measurement noise.

II. PROBLEM FORMULATION

The photovoltaic (PV) system and the wind generation system, specifically the permanent magnet synchronous generator

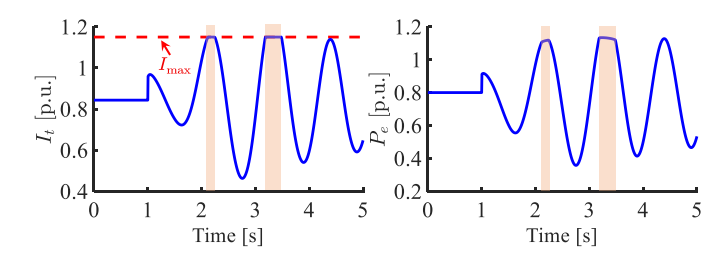


Fig. 2. Dynamic response of VSG after a disturbance. (a) Terminal current magnitude; (b) Active power.

(PMSG) system, are predominant IBRs that offer virtual inertia. Rather than determining virtual inertia from an individual unit, this paper focuses on estimating aggregated virtual inertia for efficient transmission system operation. While manufacturers may provide inertia and damping parameters for each individual IBR unit, the equivalent value for the entire IBR system remains uncertain, especially when the inertia of IBRs is time-varying since these characteristics can stabilize the system and limit the power flow of inverter [22]. As a result, estimating inertia and damping factor from aggregated IBRs is still necessary.

Once IBRs are equipped with VSG control, as shown in Fig. 1, they can provide frequency support. In Fig. 1, P_e and P_{set} denote the active power of IBR and its reference value; Note that, P_{set} is equal to the active power output of IBR at the steady state; $\vec{I}_t = I_t \angle \psi$ is the terminal current, while I_t' is the current limited by VSG; $\vec{V}_s = V_s \angle \delta$ represents the internal voltage inside VSG; \vec{V}_{lim} is the voltage limited by VSG to make sure that the voltage drop on IBR won't exceed the maximum value; the measured terminal voltage of IBR and its reference value are represented by $\vec{V}_t = V_t \angle \theta$ and V_{set} severally; $\vec{Z}_v = R_v + jX_v$ is the virtual impedance, and $\vec{Z}_s = R_s + jX_s$ is the converter series impedance; K_p and K_i are the voltage control module parameters.

The control framework of VSG contains three modules: active power control, voltage control and current limiter control. The critical module of VSG is active power control to render virtual inertia for frequency deviation mitigation. It is

$$\begin{cases} \frac{d\delta}{dt} = \Delta\omega = \omega - \omega_s \\ \frac{d\omega}{dt} = \frac{1}{T_a} \left(P_{set} - P_e - D_p \bigtriangleup \omega \right) \end{cases}$$
 where ω denotes the virtual frequency and ω_s is the synchro-

nization frequency; T_a is the virtual inertia while D_p is the damping factor. There are two main challenges:

- (1) shows highly nonlinear property due to including P_e , which is calculated via \vec{V}_s , \vec{V}_t and the equivalent impedance between them. Time-varying T_a and unknown D_{v} further increase the difficulty in estimating inertia and damping factor. Although [20] has developed a time-varying inertia estimation method, it suffers from numerical oscillations;
- · As an inverter cannot tolerate very high current, it is equipped with the current limiter, i.e.,

$$\vec{V}_{lim} = \vec{V}_t + \vec{Z}_s \vec{I}_t' \tag{2}$$

$$\vec{V}_{lim} = \vec{V}_t + \vec{Z}_s \vec{I}_t^{\dagger}$$

$$\vec{I}_t^{\prime} = I_{lim}(\vec{I}_t) = \begin{cases} I_t \angle \psi & I_t \le I_{max} \\ I_{max} \angle \psi & I_t > I_{max} \end{cases}$$
(3)

3

In (3), I_{max} is the maximum current that the inverter can tolerate, and $I_{lim}(\cdot)$ is the current limiter function. As shown in Fig. 2, the current limiter is activated when IBRs experience over-current conditions beyond permissible levels. Specifically, when the current surpasses the maximum tolerance threshold of the IBRs, the limiter engages to restrict the current at a defined ceiling value until the current is smaller. The likelihood of such large currents is related to the type and location of the disturbance. For example, three-phase short-circuit fault is a typical disturbance that leads to large currents. Besides, if a disturbance is close to the IBRs, this also can result in large current. As a result, the current limiter in IBRs is triggered. From (2) to (3), it can be seen that the power will be blocked when the current limiter is activated, leading to failure in providing virtual inertia. Note that, the orange area is the stage where the current limiter acts. Therefore, if the effects of the current limiter are not considered, inertia tracking results will be biased. How to deal with these effects for inertia estimation is still an open problem.

Remark: The fundamental component of VSG control is the active power control based on the swing equation, which is essential for mimicking the inertial response of a synchronous generator. Besides active power control, the implemented VSG control scheme incorporates a virtual automatic voltage regulator for voltage control. While advanced high-order VSG controls introducing additional elements, such as virtual governors or inner-outer loop controls, have been developed [23], [24], the swing equation-based active power control remains an indispensable element. This allows for conducting inertia estimation. Consequently, the model depicted in Fig. 1 is an appropriate representation of a typical VSG control.

III. PROPOSED VBAUKF FOR IBR INERTIA ESTIMATION

A. Virtual Frequency Estimation

From (1), it can be seen that, if ω is known, (1) is tractable. Thus, the first step is estimating the VSG's virtual frequency ω , which is achieved by Thevenin equivalent in this paper. Specifically, the internal voltage of VSG can be derived as:

$$\vec{V}_{s} = V_{sr} + jV_{si} = \vec{V}_{t} + \vec{Z}_{e}\vec{I}_{t}
= \vec{V}_{t} + (R_{e} + jX_{e})\vec{I}_{t}
= (V_{tr} + jV_{ti}) + (R_{e} + jX_{e})(I_{tr} + jI_{ti})$$
(4)

where $\vec{Z}_e = R_e + jX_e = Z_e \angle \phi$, $R_e = R_v + R_s$ and $X_e = X_v + X_s$. The real and imaginary components of relevant variables are indicated by the subscripts "r" and "i" respectively. Considering the difference between two continuous measurements, (4) is reformulated into the matrix form:

$$\begin{bmatrix} -\Delta I_{tr} & \Delta I_{ti} \\ -\Delta I_{ti} & -\Delta I_{tr} \end{bmatrix} \begin{bmatrix} R_e \\ X_e \end{bmatrix} = \begin{bmatrix} \Delta V_{tr} \\ \Delta V_{ti} \end{bmatrix} - \begin{bmatrix} \Delta V_{sr} \\ \Delta V_{si} \end{bmatrix}$$
(5)

Taking $[\Delta V_{sr} \ \Delta V_{si}]^{\mathsf{T}}$ as estimation error e, (5) can be rewritten as:

$$\begin{pmatrix}
\begin{bmatrix}
-\Delta I_{tr} & \Delta I_{ti} \\
-\Delta I_{ti} & -\Delta I_{tr}
\end{bmatrix} + e
\end{pmatrix}
\begin{bmatrix}
R_e \\
X_e
\end{bmatrix} + \eta = \begin{bmatrix}
\Delta V_{tr} \\
\Delta V_{ti}
\end{bmatrix} (6)$$

where η is the measurement noises. Since (6) is a linear equation, it can be solved by recursive total least squares [6]. Once R_s and X_s are estimated, $\vec{V_s} = V_s \angle \delta$ can be calculated with (4). Consequently, the virtual frequency of VSG can be obtained as $\omega = d\delta/dt$. With the obtained ω , it is feasible

to estimate unknown parameters T_a and D_p using a real-time nonlinear estimator.

B. Parameter Estimation Model Derivation

In our previous work [6], an unscented Kalman filter is employed to identify the inertia constant for SG. However, it neglects the damping factor and impedance of SG, which will yield a large estimation bias. Therefore, in this paper, a more comprehensive model is derived.

To track inertia accurately, (1) is utilized together with nonlinear P_e and reactive power Q_e :

$$\begin{cases}
P_e = \frac{V_s V_t}{Z_e} \cos(\theta - \delta + \phi) - \frac{V_t^2}{Z_e} \cos(\phi) \\
Q_e = \frac{V_s V_t}{Z_e} \sin(\theta - \delta + \phi) - \frac{V_t^2}{Z_e} \sin(\phi)
\end{cases}$$
(7)

Employing both functions of active and reactive power, as opposed to just one, introduces redundancy, thereby diminishing uncertainty and enhancing the reliability of inertia estimation. Through adding V_s , T_a and D_p to be extra unknown variables, (1) and (7) are merged within the Kalman filter framework, in which the discrete differential equations are derived as:

$$\begin{cases} \omega_{k} - \omega_{k-1} = \frac{\Delta t}{T_{a,k-1}} \left[P_{set} - \tilde{P}_{e,k-1} - D_{k-1} \triangle \omega_{k-1} \right] + \epsilon_{k1} \\ \delta_{k} - \delta_{k-1} = (\omega_{k-1} - \omega_{s}) \Delta t + \epsilon_{k2} \\ V_{s,k} = V_{s,k-1} + \epsilon_{k3} \\ T_{a,k} = T_{a,k-1} + \epsilon_{k4} \\ D_{p,k} = D_{p,k-1} + \epsilon_{k5} \end{cases}$$
(8)

$$\tilde{P}_{e,k} = \frac{V_{s,k}V_{t,k}}{Z_{e,k}}\cos(\theta_{k-1} - \delta_{k-1} + \phi_k) - \frac{V_{t,k}^2}{Z_{e,k}}\cos(\phi_k)$$
(9)

where k is the time step. The active power of IBRs equal to P_{set} under the steady operation due to the active power control module. Therefore, P_{set} can be obtained via the pre-fault active power of IBRs. In addition, since the virtual frequency ω can be estimated, the discrete measurement functions are formulated for ω , P_e and Q_e at time step k simultaneously:

$$\begin{cases} z_{k1} = \frac{d\delta}{dt} = \omega_k + \upsilon_{k1} \\ z_{k2} = \frac{V_{s,k}V_{t,k}}{Z_{e,k}} \cos(\theta_k - \delta_k + \phi_k) - \frac{V_{t,k}^2}{Z_{e,k}} \cos(\phi_k) + \upsilon_{k2} \\ z_{k3} = \frac{V_{s,k}V_{t,k}}{Z_{e,k}} \sin(\theta_k - \delta_k + \phi_k) - \frac{V_{t,k}^2}{Z_{e,k}} \sin(\phi_k) + \upsilon_{k3} \end{cases}$$
(10)

In (8)-(10), Δt is the sampling time interval; z_{k2} and z_{k3} represent correspondingly the measurement functions of active and reactive power; the zero-mean white Gaussian process noise $\epsilon_{\mathbf{k}} = [\epsilon_{k1} \ \epsilon_{k2} \ \epsilon_{k3} \ \epsilon_{k4} \ \epsilon_{k5}]^{\mathsf{T}}$ and measurement noise $\mathbf{v}_{\mathbf{k}} = [v_{k1} \ v_{k2} \ v_{k3}]^{\mathsf{T}}$ have covariance $\mathbf{Q}_k = \mathrm{E}[\epsilon_k \epsilon_k^{\mathsf{T}}]$ as well as $\mathbf{R}_k = \mathrm{E}[v_k v_k^{\mathsf{T}}]$ severally.

According to (8)-(10), it can be conjectured that the discrete inertia tracking model is nonlinear and time-varying under the unknown T_a and D_p . This paper proposes the VBAUKF method to deal with that. For more compact expressions, (8) and (10) are respectively denoted by the discretized state function $f(\cdot)$ and measurement functions $h(\cdot)$:

$$\begin{cases} x_k = f(x_{k-1}, u_k) + \epsilon_k \\ z_k = h(x_k, u_k) + \upsilon_k \end{cases}$$
(11)

in (11), $x \in \mathbb{R}^{n \times 1}$ and $z \in \mathbb{R}^{m \times 1}$ denote respectively the state and measurement vector, while n and m represent their corresponding dimensions. $u = [P_{set} \ V_t \ \theta]^{\mathsf{T}}$ is

the input. In addition, x_k is equivalently represented via $[\omega_k \ \delta_k \ V_{s,k} \ T_{a,k} \ D_{p,k}]^\mathsf{T}$, while z_k can be denoted by

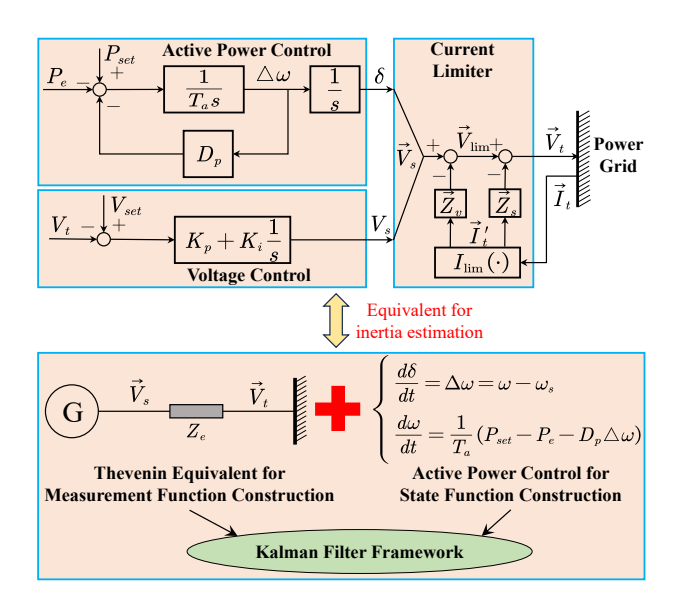


Fig. 3. VSG control equivalent for inertia estimation

Remark: As illustrated in Fig. 3, the Thevenin equivalent of IBRs and active power control are integral to constructing the Kalman filter framework for inertia estimation. The proposed method primarily utilizes the internal voltage V_s , employed in the measurement function for active and reactive power derivation, without relying on control information from the voltage control module. Consequently, the control strategy or efficacy of voltage regulation does not influence the estimation's accuracy, as the method calculates the active and reactive power of IBRs based on V_s , irrespective of its specific values. C. VBAUKF-based Inertia and damping factor Estimation

[25] presented the generalized maximum-likelihood UKF (GM-UKF) to better manage outliers, while [26] developed the H-infinity UKF specifically to address inaccuracies in model parameters, addressing model uncertainties. Despite these advancements, a common shortfall in these approaches is their limited capability in managing noise uncertainties. This is primarily due to the process noise and measurement covariance matrices being statically determined based on empirical data in [25], [26], without accommodating changes over time.

In the realistic power system, the process and measurement noises are time-varying and unknown, causing challenges for accuracy estimation. To deal with this, VBAUKF is proposed, which consists of three parts: sigma points generation, construction of covariance prior distribution and variational approximations. UKF is chosen in this study for its balance between performance and computational efficiency, a notable advantage over alternatives like the extended Kalman filter, quadrature Kalman filter, and cubature Kalman filter, which typically involve greater computational demands or numerical issues [27]–[29].

1) Sigma Points Generation: At time step k, 2n sigma points χ_{k-1} can be first obtained based on the estimated state vector \hat{x}_{k-1} as well as its covariance matrix is $\sum_{k=1}^{xx}$:

$$\chi_{k-1}^{j} = \widehat{x}_{k-1} \pm \left(\sqrt{n\Sigma_{k-1}^{xx}}\right)_{j}, j = 1, 2, \dots, 2n$$
(12)

in (12), $\left(\sqrt{n\Sigma_{k-1}^{xx}}\right)_j$ denotes j-th column of $\sqrt{n\Sigma_{k-1}^{xx}}$. By transforming χ_{k-1} with $f(\cdot)$, its corresponding transformed outputs $\chi^{j}_{k|k-1}$ are calculated via:

$$\chi_{k|k-1}^{j} = f(\chi_{k-1}^{j})$$
 (13)

 $\chi_{k|k-1}^{j} = f(\chi_{k-1}^{j})$ (13) Consequently, the predicted state vector $\widehat{\boldsymbol{x}}_{k|k-1}$ is derived as:

$$\widehat{x}_{k|k-1} = \sum_{j=1}^{2n} w_j \chi_{k|k-1}^j$$
 (14)

 $w_i = 1/(2n)$ denotes the weight of j-th sigma point. The covariance matrix of $\widehat{x}_{k|k-1}$ is obtained as:

$$\Sigma_{k|k-1}^{xx} = \sum_{j=1}^{2n} w_j \left(\chi_{k|k-1}^j - \hat{x}_{k|k-1} \right) \left(\chi_{k|k-1}^j - \hat{x}_{k|k-1} \right)^\mathsf{T} + Q_k$$
(15)

2) Construction of Covariance Prior Distribution: In (15), since there is no precise knowledge about Q_k , $\Sigma_{k|k-1}^{xx}$ is inaccurate while the similar scenario is also applied to R_k , leading to tremendous tracking errors or algorithm divergence. To get the accurate posterior distribution of $\Sigma_{k|k-1}^{xx}$ and R_k , the prior distribution of Q_k , $\Sigma_{k|k-1}^{xx}$ and R_k should be defined.

It is an assumption that both the conditional distribution $p(\boldsymbol{x}_k \mid \boldsymbol{z}_{1:k-1})$ and the likelihood $p(\boldsymbol{z}_k \mid \boldsymbol{x}_k)$ obey Gaussian distribution:

$$p\left(\boldsymbol{x}_{k} \mid \boldsymbol{z}_{1:k-1}, \boldsymbol{\Sigma}_{k|k-1}^{xx}\right) = \mathcal{N}(\boldsymbol{x}_{k}; \widehat{\boldsymbol{x}}_{k|k-1}, \boldsymbol{\Sigma}_{k|k-1}^{xx}) \quad (16)$$
$$p\left(\boldsymbol{z}_{k} \mid \boldsymbol{x}_{k}, \boldsymbol{R}_{k}\right) = \mathcal{N}\left(\boldsymbol{z}_{k}; \boldsymbol{h}(\boldsymbol{x}_{k}), \boldsymbol{R}_{k}\right) \quad (17)$$

 $z_{1:k-1}$ means measurements obtained from time step 1 to k-1; $\mathcal{N}(\cdot; \boldsymbol{\mu}, \boldsymbol{\Sigma})$ stands for Gaussian distribution, in which μ denotes the mean value and Σ represents the covariance matrix.

Targeting at deriving the joint distribution of x_k , $\Sigma_{k|k-1}^{xx}$ and R_k based on (16) and (17), the conjugate prior distribution is chosen for $\Sigma_{k|k-1}^{xx}$ and R_k . This is because the posterior and prior distributions have a similar mathematical expression if conjugacy is applied. In the Bayesian inference field, the inverse Wishart (IW) distribution can be commonly selected to be the conjugate prior distribution for the covariance matrix of a Gaussian distribution [30]. IW distribution's probability density function (PDF) of a symmetric positive definite matrix $A \in \mathbb{R}^{d \times d}$ can be written as:

$$A \in \mathbb{R}^{d \times d}$$
 can be written as:

$$IW(A; \lambda, \Upsilon) = \frac{|\Upsilon|^{\lambda/2} |A|^{-(\lambda+d+1)/2} \exp\left\{-0.5 \operatorname{tr} \left(\Upsilon A^{-1}\right)\right\}}{2^{d\lambda/2} \Gamma_d(\lambda/2)}$$
(18)

 λ represents degrees of freedom (DoF); $\boldsymbol{\Upsilon} \in \mathbb{R}^{d \times d}$ means the inverse scale matrix and d denotes its dimension; $tr(\cdot)$ is the trace function, while $\Gamma(\cdot)$ represents the d-variate gamma function. There is an important property of IW distribution for the subsequent derivations:

$$\begin{cases}
\hat{\boldsymbol{A}} \sim \text{IW}(\boldsymbol{A}; \lambda, \boldsymbol{\Upsilon}) \\
\text{E} \left[\boldsymbol{A}^{-1}\right] = (\lambda - d - 1)\boldsymbol{\Upsilon}^{-1} \text{ if } \lambda > d + 1
\end{cases}$$
(19)

According to (16) and (17), $\Sigma_{k|k-1}^{xx}$ and R_k represent respectively the covariance matrices of Gaussian distributions. Consequently, prior distributions of them can be formulated

as:
$$\begin{cases}
p(\boldsymbol{\Sigma}_{k|k-1}^{xx} \mid \boldsymbol{z}_{1:k-1}) = IW(\boldsymbol{\Sigma}_{k|k-1}^{xx}; \widehat{t}_{k|k-1}, \widehat{\boldsymbol{T}}_{k|k-1}) \\
p(\boldsymbol{R}_k \mid \boldsymbol{z}_{1:k-1}) = IW(\boldsymbol{R}_k; \widehat{u}_{k|k-1}, \widehat{\boldsymbol{U}}_{k|k-1})
\end{cases} (20)$$

where $\hat{t}_{k|k-1}$ and $\hat{u}_{k|k-1}$ are respectively the DoF parameters for $p(\Sigma_{k|k-1}^{xx} \mid z_{1:k-1})$ and $p(R_k \mid z_{1:k-1})$, while $T_{k|k-1}$ and $U_{k|k-1}$ denotes their inverse scale matrices accordingly.

To obtain the prior parameters $\hat{t}_{k|k-1}$, $\hat{u}_{k|k-1}$, $\hat{T}_{k|k-1}$ and $\widehat{m{U}}_{k|k-1},$ (19) is utilized. Specifically, let $\widehat{m{\Sigma}}_{k|k-1}^{xx}$ be the mean value of $\Sigma_{k|k-1}^{xx}$ and Q_k be the mean value of Q_k , we get:

$$\frac{\widehat{T}_{k|k-1}}{\widehat{t}_{k|k-1} - n - 1} = \widehat{\Sigma}_{k|k-1} \tag{21}$$

where,

$$\widehat{\boldsymbol{\Sigma}}_{k|k-1}^{xx} = \sum_{j=1}^{2n} w_j \left(\boldsymbol{\chi}_{k|k-1}^j - \widehat{\boldsymbol{x}}_{k|k-1} \right) \left(\boldsymbol{\chi}_{k|k-1}^j - \widehat{\boldsymbol{x}}_{k|k-1} \right)^\mathsf{T} + \widehat{\boldsymbol{Q}}_k$$
(22)

Define $\hat{t}_{k|k-1} = n + \tau + 1$, in which $\tau \geqslant 0$ denotes a hyperparameter. As a result, $\widehat{T}_{k|k-1}$ is derived as:

$$\widehat{T}_{k|k-1} = \tau \widehat{\Sigma}_{k|k-1} \tag{23}$$

Since the measurement noises are varying the previous posteriors $p\left(\boldsymbol{R}_{k-1}\mid\boldsymbol{z}_{1:k-2}\right)=\operatorname{IW}\left(\boldsymbol{R}_{k-1};\widehat{u}_{k-1\mid k-2},\widehat{\boldsymbol{U}}_{k-1\mid k-2}\right)$ can be propagated in time by means of a adjustment factor $\rho_u \in [0 \ 1]^T$ [31]. Consequently, prior parameters of $p(\mathbf{R}_k \mid \mathbf{z}_{1:k-1})$ are obtained:

$$\begin{cases} \widehat{u}_{k|k-1} = \rho_u \left(\widehat{u}_{k-1|k-2} - m - 1 \right) + m + 1 \\ \widehat{U}_{k|k-1} = \rho_u \widehat{U}_{k-1|k-2} \end{cases}$$
(24)

3) Variational Approximations for Covariance Poste*rior Distribution*: Once the prior distributions of $\Sigma_{k|k-1}^{xx}$ and R_k are determined, the union posterior distribution $p(\boldsymbol{x}_k, \boldsymbol{\Sigma}_{k|k-1}^{xx}, \boldsymbol{R}_k \mid \boldsymbol{z}_{1:k})$ should be solved so that $\boldsymbol{x}_k, \boldsymbol{\Sigma}_{k|k-1}^{xx}$ and R_k can be inferred simultaneously. However, it is hard to formulate the analytical form. Therefore, the variational approximation (VB) can be utilized to deduce a factored PDF to approximate $p(\boldsymbol{x}_k, \boldsymbol{\Sigma}_{k|k-1}^{xx}, \boldsymbol{R}_k \mid \boldsymbol{z}_{1:k})$:

 $p(\boldsymbol{x}_k, \boldsymbol{\Sigma}_{k|k-1}^{xx}, \boldsymbol{R}_k \mid \boldsymbol{z}_{1:k}) \approx q(\boldsymbol{x}_k) q(\boldsymbol{\Sigma}_{k|k-1}^{xx}) q(\boldsymbol{R}_k)$ where $q(x_k)$, $q(\Sigma_{k|k-1}^{xx})$ and $q(R_k)$ are respectively approximated posterior distribution of x_k , $\Sigma_{k|k-1}^{xx}$ and R_k .

The core idea of VB to perform (25) minimizing Kullback-Leibler divergence (KLD) between $p(\boldsymbol{x}_k, \boldsymbol{\Sigma}_{k|k-1}^{xx}, \boldsymbol{R}_k \mid \boldsymbol{z}_{1:k})$ and $q(\boldsymbol{x}_k)q(\boldsymbol{\Sigma}_{k|k-1}^{xx})q(\boldsymbol{R}_k)$ via iterations, whose objective function is defined as:

 $\vartheta^{\star}(\cdot) = argmin \ \underset{\vartheta(\cdot)}{\mathrm{KLD}}(\vartheta \| p) \equiv \int \vartheta(\cdot) \log \frac{\vartheta(\cdot)}{p(\cdot)} d(\cdot)$ where $p(\cdot) = p(\boldsymbol{x}_k, \boldsymbol{\Sigma}_{k|k-1}^{xx}, \boldsymbol{R}_k \mid \boldsymbol{z}_{1:k})$ and $\vartheta(\cdot) =$ $q(\boldsymbol{x}_k)q(\boldsymbol{\Sigma}_{k|k-1}^{xx})q(\boldsymbol{R}_k)$. Solving (26) is equivalent to iterating the following equations:

where
$$\Xi = \{x_k, \Sigma_{k|k-1}^{xx}, R_k\}$$
 and $\xi \in \Xi$; c_{ξ} is a constant,

while $\Xi^{(-\xi)}$ denotes removing ξ from Ξ ; $p(\Xi, z_{1:k})$ is the joint PDF of Ξ and $z_{1:k}$; $E(\cdot)$ denotes the expectation function. Consequently, the predicted posterior mean state vector's covariance $\widehat{\Sigma}_{k|k-1}^{xx,(i+1)}$ and the posterior mean measurement noise covariance $\widehat{R}_k^{(i+1)}$ are obtained via:

$$\begin{cases} G_{k}^{(i)} = \Sigma_{k}^{xx,(i)} + \left(\widehat{x}_{k}^{(i)} - \widehat{x}_{k|k-1}\right) \left(\widehat{x}_{k}^{(i)} - \widehat{x}_{k|k-1}\right)^{\mathsf{T}} \\ B_{k}^{(i)} = \Sigma_{k}^{zz,(i)} + \left(z_{k} - h(\widehat{x}_{k}^{(i)})\right) \left(z_{k} - h(\widehat{x}_{k}^{(i)})\right)^{\mathsf{T}} \\ \widehat{\Sigma}_{k|k-1}^{xx,(i+1)} = \widehat{T}_{k}^{(i+1)} / (\widehat{t}_{k}^{(i+1)} - n - 1) \end{cases}$$

$$\text{where } \widehat{t}_{k}^{(i+1)} = \widehat{t}_{k|k-1} + 1, \quad \widehat{T}_{k}^{(i+1)} = G_{k}^{(i)} + \\ \widehat{T}_{k|k-1}; \quad \Sigma_{k}^{xx,(i)} = \mathbf{E} \left[\left(x_{k} - \widehat{x}_{k}^{(i)}\right) \left(x_{k} - \widehat{x}_{k}^{(i)}\right)^{\mathsf{T}} \right]; \widehat{\Sigma}_{k}^{zz,(i)} = \\ \mathbf{E} \left[\left(h(\widehat{x}_{k}^{(i)}) - h(x_{k})\right) \left(h(\widehat{x}_{k}^{(i)}) - h(x_{k})\right)^{\mathsf{T}} \right].$$

$$\widehat{R}_{k}^{(i+1)} = \frac{\widehat{U}_{k}^{(i+1)}}{(\widehat{u}_{k}^{(i+1)} - m - 1)}$$

$$= \frac{\rho_{u}(\widehat{u}_{k-1} - m - 1) \widehat{R}_{k-1} + \mathbf{B}_{k}^{(i)}}{\rho_{u}(\widehat{u}_{k-1} - m - 1) + 1}$$

$$\text{where } \widehat{u}_{k}^{(i+1)} = \widehat{u}_{k|k-1} + 1 \text{ and } \widehat{U}_{k}^{(i+1)} = \mathbf{B}_{k}^{(i)} + \widehat{U}_{k|k-1}.$$

Recall that there is no analytical form for $\Sigma_k^{zz,(i)}$ in (28), we employ the following formula to approximate $\widehat{R}_k^{(i+1)}$ if current limiter is not activated:

$$\widehat{\boldsymbol{R}}_{k}^{(i+1)} = \rho \widehat{\boldsymbol{R}}_{k-1} + (1-\rho)\boldsymbol{d}_{k}\boldsymbol{d}_{k}^{\mathsf{T}}$$
(30)

where d_{k-1} represents the innovation error at time k-1 and ρ is a value between [0 1]. If the current limiter is activated, $\Sigma_k^{zz,(i)}$ can be approximated via sigma points:

$$\begin{cases}
(\boldsymbol{\chi}_{k}^{j})^{(i)} = \widehat{\boldsymbol{x}}_{k}^{(i)} \pm \left(\sqrt{n\boldsymbol{\Sigma}_{k|k}^{xx,(i)}}\right)_{j}, j = 1, 2, \cdots, 2n \\
(\boldsymbol{\mathcal{Z}}_{k}^{j})^{(i)} = \boldsymbol{h}((\boldsymbol{\chi}_{k}^{j})^{(i)}), \widehat{\boldsymbol{z}}_{k}^{(i)} = \sum_{j=1}^{2n} w_{j}(\boldsymbol{\mathcal{Z}}_{k}^{j})^{(i)} \\
\boldsymbol{\Sigma}_{k}^{zz,(i)} \approx \sum_{j=1}^{2n} w_{j} \left(\boldsymbol{h}((\boldsymbol{\mathcal{Z}}_{k}^{j})^{(i)}) - \widehat{\boldsymbol{z}}_{k}^{(i)}\right) \left(\boldsymbol{h}((\boldsymbol{\mathcal{Z}}_{k}^{j})^{(i)}) - \widehat{\boldsymbol{z}}_{k}^{(i)}\right)^{\mathsf{T}}
\end{cases} \tag{31}$$

Exploiting (28)-(29), $q^{(i+1)}(x_k)$ is derived as:

$$q^{(i+1)}(\boldsymbol{x}_k) = \mathcal{N}(\boldsymbol{x}_k; \widehat{\boldsymbol{x}}_k^{(i+1)}, \boldsymbol{\Sigma}_k^{xx,(i+1)})$$
(32)

 $q^{(i+1)}(\boldsymbol{x}_k) = \mathcal{N}(\boldsymbol{x}_k; \widehat{\boldsymbol{x}}_k^{(i+1)}, \boldsymbol{\Sigma}_k^{xx,(i+1)}) \tag{32}$ In (32), $\widehat{\boldsymbol{x}}_k^{(i+1)}$ and $\boldsymbol{\Sigma}_k^{xx,(i+1)}$ are derived according to the following measurement updating process, which is same as that in standard UKF:

$$\begin{cases} (\boldsymbol{\chi}_{k|k-1}^{j})^{(i+1)} = \widehat{\boldsymbol{x}}_{k|k-1} \pm \left(\sqrt{n}\widehat{\boldsymbol{\Sigma}}_{k|k-1}^{xx,(i+1)}\right)_{j}, j = 1, \cdots, 2n \\ (\boldsymbol{\mathcal{Z}}_{k|k-1}^{j})^{(i+1)} = \boldsymbol{h}((\boldsymbol{\chi}_{k|k-1}^{j})^{(i+1)}) \\ \widehat{\boldsymbol{z}}_{k|k-1}^{(i+1)} = \sum_{j=1}^{2n} w_{j}(\boldsymbol{\mathcal{Z}}_{k|k-1}^{j})^{(i+1)} \\ (\boldsymbol{e}_{k|k-1}^{zz,j})^{(i+1)} = \boldsymbol{h}((\boldsymbol{\chi}_{k|k-1}^{j})^{(i+1)}) - \widehat{\boldsymbol{z}}_{k|k-1}^{(i+1)} \\ \boldsymbol{\Sigma}_{k|k-1}^{zz,(i+1)} = \sum_{j=1}^{2n} w_{j}(\boldsymbol{e}_{k|k-1}^{zz,j})^{(i+1)} \left((\boldsymbol{e}_{k|k-1}^{zz,j})^{(i+1)} \right)^{\mathsf{T}} + \widehat{\boldsymbol{R}}_{k}^{(i+1)} \\ (\boldsymbol{e}_{k|k-1}^{xx,j})^{(i+1)} = (\boldsymbol{\chi}_{k|k-1}^{j})^{(i+1)} - \widehat{\boldsymbol{x}}_{k|k-1} \\ \boldsymbol{\Sigma}_{k|k-1}^{xz,(i+1)} = \sum_{j=1}^{2n} w_{j}(\boldsymbol{e}_{k|k-1}^{xx,j})^{(i+1)} \left((\boldsymbol{e}_{k|k-1}^{xz,j})^{(i+1)} \right)^{\mathsf{T}} \\ \boldsymbol{K}_{k}^{(i+1)} = \boldsymbol{\Sigma}_{k|k-1}^{xz,(i+1)} (\boldsymbol{\Sigma}_{k|k-1}^{zz,(i+1)})^{-1} \\ \widehat{\boldsymbol{x}}_{k}^{(i+1)} = \widehat{\boldsymbol{x}}_{k|k-1} + \boldsymbol{K}_{k}^{(i+1)} (\boldsymbol{z}_{k} - \widehat{\boldsymbol{z}}_{k|k-1}^{(i+1)}) \\ \boldsymbol{\Sigma}_{k}^{xx,(i+1)} = \widehat{\boldsymbol{\Sigma}}_{k|k-1}^{xx,(i+1)} + \boldsymbol{K}_{k}^{(i+1)} \boldsymbol{\Sigma}_{k|k-1}^{zz,(i+1)} \left(\boldsymbol{K}_{k}^{(i+1)} \right)^{\mathsf{T}} \end{cases}$$

After N fixed-point iterations, the inference of the posterior distribution of time-varying $\Sigma_{k|k-1}^{xx}$ and R_k can converge.

The residual d_k is obtained by $z_k - \widehat{z}_{k|k-1}^N$. In this paper, $\widehat{x}_k = \widehat{x}_k^{(N)}$ and $\Sigma_k^{xx} = \Sigma_k^{xx,(N)}$ are respectively used as the final estimated state and its corresponding mean covariance matrix at time step k, while $\widehat{R}_k = \widehat{R}_k^N$ represents the mean measurement noise covariance. To further improve the posterior inference speed and accuracy, Q_k can be updated according to (34). This allows providing a good prior mean value for Q_k .

$$\begin{cases}
\boldsymbol{C}_{k} = \frac{\sum_{i=k-L+1}^{k} (\boldsymbol{z}_{i} - \boldsymbol{h}(\widehat{\boldsymbol{x}}_{i}))(\boldsymbol{z}_{i} - \boldsymbol{h}(\widehat{\boldsymbol{x}}_{i}))^{\mathsf{T}}}{L} \\
\alpha = (1-\beta)/(1-\beta^{k}) \\
\widehat{\boldsymbol{Q}}_{k+1} = (1-\alpha)\widehat{\boldsymbol{Q}}_{k} + \alpha \mathbf{K}_{k}^{(N)} \boldsymbol{C}_{k} \left(\mathbf{K}_{k}^{(N)}\right)^{\mathsf{T}}
\end{cases} (34)$$

where L is the length of the measurements to update Q_k and $\beta \in [0.95\ 1]^\mathsf{T}$ is a constant. In this way, the memory of old Q_k can be exponentially released while Q_k is updated with recent measurements.

D. Inertia Estimation Framework with Current Limiter

During the effects of the current limiter, there is an estimation error of the equivalent impedance \vec{Z}_e of VSG if measurements are kept, but these measurements can be utilized. This is because if the measurements during the activation of the current limiter are thrown away, the performance of the proposed inertia estimator may deteriorate due to the large discontinuities. Therefore, in this paper, the measurements during the activation of the current limiter are used. From Fig. 2, it is evident that when the disturbance current surpasses the maximum threshold, the current value is maintained at this maximum. This effectively halts energy output to the grid, leading to a situation where both virtual inertia and damping factor are nullified. Given this behavior, the equivalent inertia $H = \frac{1}{2}T_a$ and damping factor can be considered zero in such scenarios. In other words, from the perspective of the IBR terminals, there are sharp fluctuations in inertia and damping factor, i.e., from a large value to zero. As a result, the only issue is the discontinuities coming from the instant when the current limiter is activated.

Since $\widehat{z}_{k-1|k-2}^N$ is the predicted value for measurements, which hasn't considered the measurement noise. Therefore, $d_{k-1} = z_{k-1} - \widehat{z}_{k-1|k-2}^N$ can be used to indicate the noise level. The adaptive change of \boldsymbol{R} via d_{k-1} allows for accurate and fast-tracking of time-varying inertia and damping factor when the current limiter is not activated. However, (30) is sensitive to sharp changes caused by the current limiter since \boldsymbol{R} is updated with the relatively large innovation error. This can lead to large estimation errors when the current limiter is activated.

It is observed that (29) is influenced by the estimation error $[z_k - h(\widehat{x}_k^{(i)})]$, calculated using the estimated states or parameters \widehat{x}_k . Given that $[z_k - h(\widehat{x}_k^{(i)})]$, which could be zero in an ideal scenario, is considerably smaller than the innovation error d_{k-1} , the estimator employing (29) demonstrates less sensitivity compared to that using (30), particularly under abrupt parameter shifts during the current limiter's activation.

Therefore, to mitigate the discontinuities at the present time step, (29) is utilized to update R_k during the activation of the

Algorithm 1: The proposed inertia estimation framework for VSG-based IBRs considering current limiter.

Input: Measurements of $\vec{V_t}$, $\vec{I_t}$, P_e and Q_e ; the time

```
instant k_{end}; \tau; \rho; N.
        Output: The equivalent inertia H and damping factor
                                D_p of VSG-based IBRs.
  1 Initialize \hat{x}_0, \Sigma_0^{xx}, R_0, Q_0;
  2 for k = 1; k \le k_{end} do
  3
                 Estimate \vec{Z}_{e,k}, \omega_k using (6) and \omega = d\delta/dt;
                 Generate sigma points using (12), (13), (14), (22);
  4
                 Update \hat{t}_{k|k-1} and \hat{T}_{k|k-1} using
  5
                    \hat{t}_{k|k-1} = n + \tau + 1 and (23);
                 Update \widehat{u}_{k|k-1} and \widehat{U}_{k|k-1} using (24);
  6
                 for i=1; i \leq N do
  7
                          \begin{array}{l} \text{Update } \overset{-}{\boldsymbol{G}}_{k}^{(i)} \text{ using (28);} \\ \text{Update } \widehat{t}_{k}^{(i+1)}, \, \widehat{\boldsymbol{T}}_{k}^{(i+1)} \colon \widehat{t}_{k}^{(i+1)} = \widehat{t}_{k|k-1} + 1, \\ \widehat{\boldsymbol{T}}_{k}^{(i+1)} = \overset{-}{\boldsymbol{G}}_{k}^{(i)} + \widehat{\boldsymbol{T}}_{k|k-1}; \end{array}
  8
   9
                         \begin{split} & \boldsymbol{T}_{k}^{i} = \boldsymbol{G}_{k}^{i} + \boldsymbol{I}_{k|k-1}, \\ & \text{Update } \boldsymbol{B}_{k}^{(i)} \text{ using (28) and (31);} \\ & \text{Update } \widehat{\boldsymbol{u}}_{k}^{(i+1)}, \widehat{\boldsymbol{U}}_{k}^{(i+1)} \colon \widehat{\boldsymbol{u}}_{k}^{(i+1)} = \widehat{\boldsymbol{u}}_{k|k-1} + 1, \\ & \widehat{\boldsymbol{U}}_{k}^{(i+1)} = \boldsymbol{B}_{k}^{(i)} + \widehat{\boldsymbol{U}}_{k|k-1}; \\ & \text{if } \textit{Current limiter is activated } \textbf{then} \\ & \mid \text{Update } \widehat{\boldsymbol{\Sigma}}_{k|k-1}^{xx,(i+1)}, \, \boldsymbol{R}_{k}^{(i+1)} \text{ by (28) and (29);} \end{split}
10
11
12
13
14
                                    Update \Sigma_{k|k-1}^{xx,(i+1)}, \widehat{\boldsymbol{R}}_{k}^{(i+1)} by (28) and (30);
15
16
                           Update \mathbf{K}_{k}^{(i+1)}, \widehat{x}_{k}^{(i+1)}, \Sigma_{k}^{xx,(i+1)} using (33);
17
18
                Update Q_k using (34); \widehat{x}_k = \widehat{x}_k^{(N)}, H_k = \frac{1}{2}T_{a,k}, \widehat{R}_k = \widehat{R}_k^N and \Sigma_k^{xx} = \Sigma_k^{xx,(N)};
19
                 if Current limiter is activated then
21
                          H_k = 0; D_{p,k} = 0;
22
23
24
                          No changes;
25
                 end
26 end
27 return H = \{H_1, H_2, \cdots, H_{k_{end}}\} and
```

current limiter. When the current limiter is not activated, (30) is employed to track time-varying inertia and damping factor. The comprehensive inertia and damping factor estimation framework with the current limiter are shown in Algorithm 1 and Fig. 4.

 $D_p = \{D_{p,1}, D_{p,2}, \cdots, D_{p,k_{end}}\}.$

Remark: In scenarios of normal operation, an array of methodologies already exist for conducting inertia estimation, such as those elucidated in references [14] and [33]. These established methods primarily leverage ambient measurements to estimate the inertia of either individual generators or the entire system. However, they are not feasible in time-varying inertia tracking under large disturbances. By contrast, our proposed method is specifically designed to address the more intricate challenge of tracking time-varying inertia during

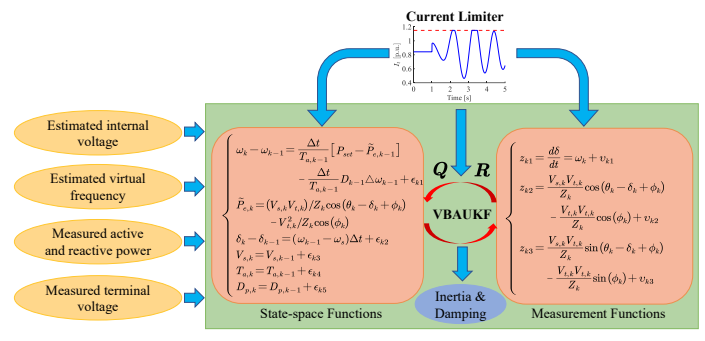


Fig. 4. Inertia and damping factor estimation framework with the current limiter

events. This distinction underscores the complementary nature of our approach in conjunction with ambient-data-based estimation methods, catering to a broader spectrum of operational scenarios.

IV. NUMERICAL RESULTS

Aiming at verifying the performance of the developed estimator, extensive simulations have been conducted on the modified IEEE 39-bus system [34], as shown in Fig. 5, and an 80-MW aggregated VSG-based IBR system is connected to Bus 4. In other words, P_{set} is equal to 80MW. The IBR system is designed to connect with a PV farm or PMSG farm that includes energy storage. Given that it's entirely isolated by the inverter, under VSG-based control, it can effectively function as a voltage source. Loads are modeled with voltage-dependency dynamic characteristics [35]. From Fig. 6, it is evident that a larger T_a results in a smaller frequency deviation. Consequently, estimating virtual inertia from IBRs proves beneficial for the power system frequency stability.

In the VSG control, K_P , K_i are respectively set as 0.5, and 0. The parameters N, ρ_u , and τ should be selected from the intervals $[6, +\infty]$, [0.9, 1], and [2, 6], respectively, as suggested in [31]. Despite our proposed nonlinear Bayesian Kalman

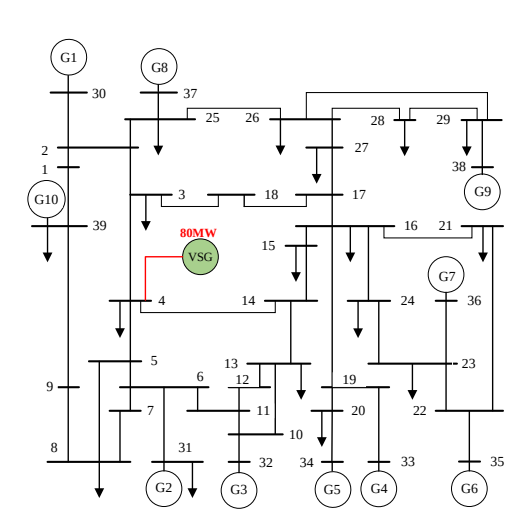


Fig. 5. The one-line diagram of modified IEEE 39-bus power system.

filter being an advancement of the linear Bayesian Kalman filter presented in [31], the parameter configurations proposed there remain applicable. For a more detailed discussion on the selection of N, ρ_u , and τ , refer to [31]. Experimental results indicate the parameters N, ρ_u , and τ exhibit negligible sensitivity to performance in terms of mitigating fluctuations attributed to the current limiter. Consequently, the values of $N=20, \ \rho_u=1-e^{-4}, \ {\rm and} \ \tau=3 \ {\rm have \ been \ adopted}$ for all testing scenarios. It is observed that L exhibits minimal sensitivity to the outcomes according to our experience. Consequently, its tuning interval can be specified as $[2, +\infty]$, with L being set to 10 in this study. β is set as 0.9999 in all testing scenarios, and its sensitivity will be discussed in Section IV-F. The diagonal elements of Σ_0^{xx} , R_0 , Q_0 are assumed to be 10^{-6} . All numerical simulations were executed using DIgSILENT PowerFactory and MATLAB/Simulink on a laptop equipped with an AMD Ryzen5 4600H processor, clocked at 3.0 GHz, and 16 GB of RAM. Note that, all disturbances occur at t = 1 s.

A. Virtual Frequency Estimation

In this subsection, the necessity of virtual frequency estimation is illustrated. The generator located at Bus 35 is disconnected at t=1 s. T_a is set as 40. Two scenarios are tested:

- Scenario A1: small impedance with $\vec{Z}_e = 0.006 + j0.106$;
- Scenario A2: large impedance with $\vec{Z}_e = 0.1 + j0.106$.

It is worth mentioning that the existing work, i.e., [4], on SG inertia estimations rely on the assumption that the terminal bus frequency can be a substitute of rotor speed. This holds for most of SG since their internal impedance is

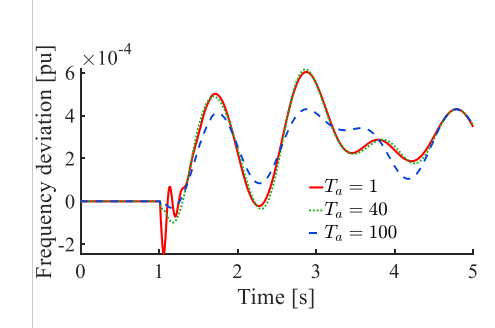


Fig. 6. Frequency deviation of Bus 40 under different T_a settings.

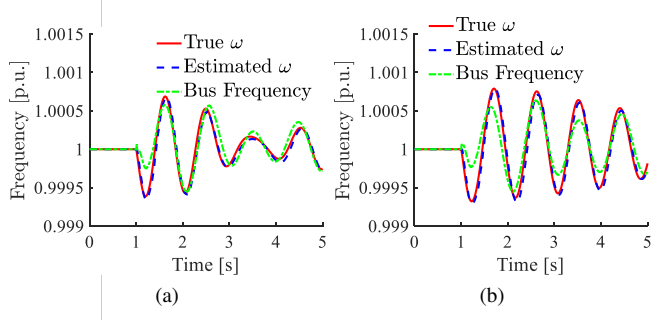


Fig. 7. Virtual frequency estimation under different scenarios. (a) Scenario A1; (b) Scenario A2.

small enough to be neglected. However, this is not the case for VSG-based inverters since a large internal impedance \vec{Z}_e may be needed to limit current. As shown in Fig. 7, the dynamic curve of the virtual frequency is different from that of the terminal bus frequency, while the dissimilarity increases as \vec{Z}_e becomes larger. Fig. 7 also presents that the proposed estimator is capable of effectively and precisely estimating the virtual frequency, which is critical for inertia tracking.

B. Inertia Estimation under Different Disturbances

To verify the robustness of the proposed inertia estimator to various disturbances, the following scenarios are considered. Specifically, the time-varying inertial control schemes in Scenarios B3 and B4 are adopted from [22]. However, to illustrate the generalization of the proposed method, a more complicated synthetic sinusoidal inertia is utilized afterward.

- Scenario B1: The generator located at Bus 35 is disconnected; Constant inertia $H=\frac{1}{2}T_a=20$ s; $\vec{Z}_e=0.006+j0.106$;
- Scenario B2: The generator located at Bus 35 is disconnected; Constant inertia $H=\frac{1}{2}T_a=20$ s; $\vec{Z}_e=0.1+j0.106$;
- Scenario B3: The generator located at Bus 35 is disconnected; Time-varying inertia $H=\frac{1}{2}T_a=25000exp(-5(50\Delta\omega+2.2))+10$ s [22]; $\vec{Z}_e=0.006+j0.106$;
- Scenario B4: The generator located at Bus 35 is disconnected; Time-varying inertia $H=\frac{1}{2}T_a=25000exp(-5(50\Delta\omega+2.2))+10$ s [22]; $\vec{Z}_e=0.1+j0.106$;
- Scenario B5: The load located at Bus 4 is disconnected; Constant inertia $H=\frac{1}{2}T_a=20$ s; $\vec{Z}_e=0.1+j0.106$;
- Scenario B6: The load located at Bus 4 is disconnected; Time-varying inertia $H=\frac{1}{2}T_a=20(sin[2\pi(t-1)]+2)$ s; $\vec{Z}_e=0.1+j0.106$;
- Scenario B7: Line 16-21 is disconnected; Constant inertia $H=\frac{1}{2}T_a=20$ s; $\vec{Z}_e=0.1+j0.106$;
- Scenario B8: Line 16-21 is disconnected; Time-varying inertia $H=\frac{1}{2}T_a=20(sin[2\pi(t-1)]+2)$ s; $\vec{Z}_e=0.1+j0.106$;

For all scenarios, 80% of T_a and D_p 's true values are used as their initial values. ρ is set as 0.95. In addition, the existing methods in [6] (M1) and [20] (M2) are taken as comparisons. In M2, T_M and T_D are set as 0.02 and 0.01 respectively. Since the damping factor is neglected in M1, the inertia estimator,

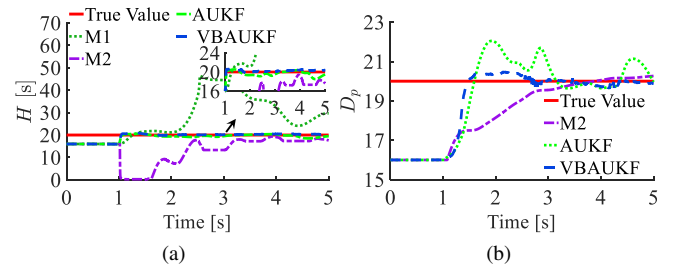


Fig. 8. Performance comparisons in Scenario B1. (a) H; (b) D_p .

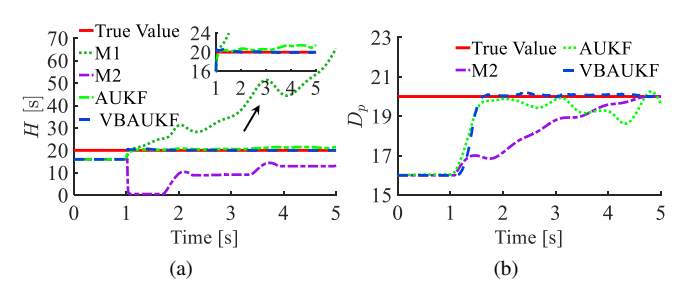


Fig. 9. Performance comparisons in Scenario B2. (a) H; (b) D_p .

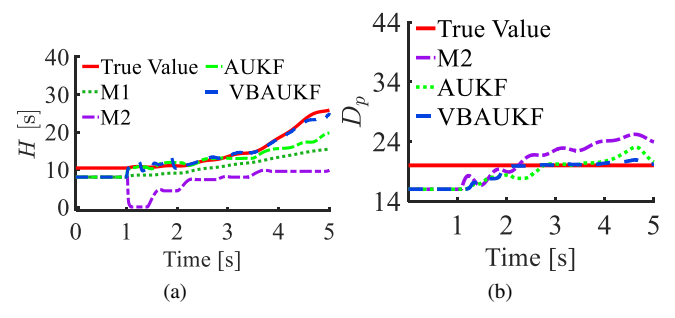


Fig. 10. Performance comparisons in Scenario B3. (a) H; (b) D_p .

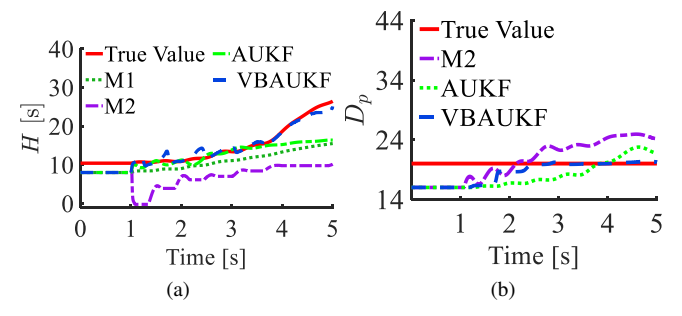


Fig. 11. Performance comparisons in Scenario B4. (a) H; (b) D_p .

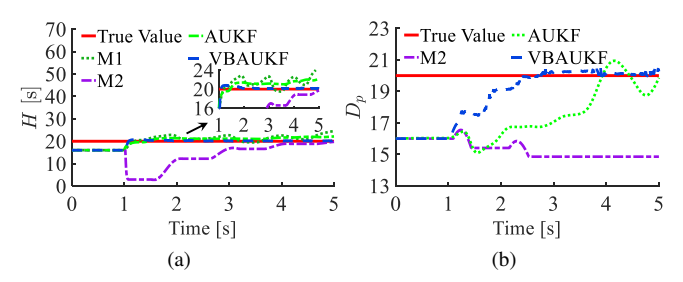


Fig. 12. Performance comparisons in Scenario B5. (a) H; (b) D_p .

adaptive unscented Kalman filter (AUKF), utilized in [6] is employed to solve (8) and (10) for comparison. This allows illustrating the importance of the damping factor and \boldsymbol{R}_k in inertia tracking. To quantify the estimation error, the maximum absolute error (MAE) and the average absolute error (AAE) after time t is formulated as:

$$MAE_{t} = \max \left\{ t' \in [t, t_{end}]; \left| \frac{\eta_{\text{true},t'} - \eta_{\text{est},t'}}{\eta_{\text{true},t'}} \right| \times 100\% \right\}$$
(35)

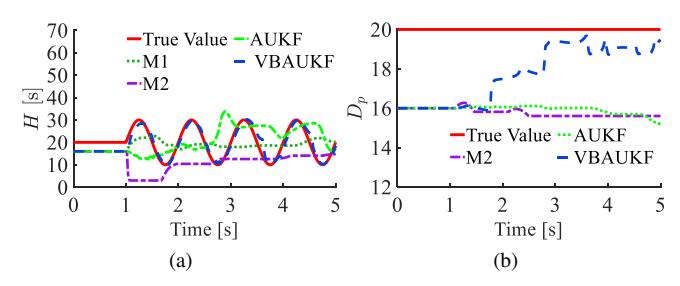


Fig. 13. Performance comparisons in Scenario B6. (a) H; (b) D_p .

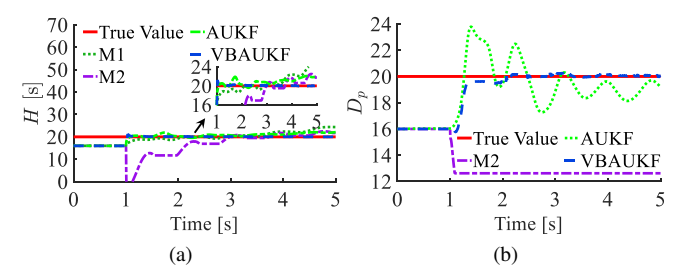


Fig. 14. Performance comparisons in Scenario B7. (a) H; (b) D_p .

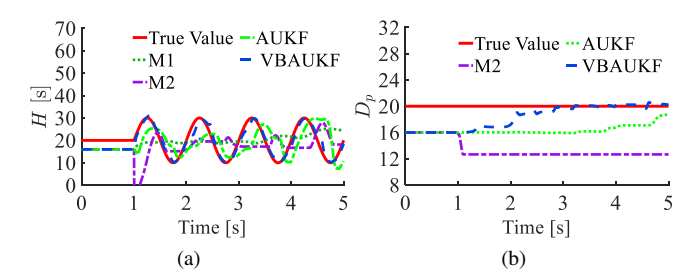


Fig. 15. Performance comparisons in Scenario B8. (a) H; (b) D_p .

$$AAE_{t} = \text{mean}\left\{t' \in [t, \ t_{end}]; \left| \frac{\eta_{\text{true},t'} - \eta_{\text{est},t'}}{\eta_{\text{true},t'}} \right| \times 100\% \right\}$$

where $\eta_{\text{true},t'}$ is the true inertia or damping factor at time t', and $\eta_{\text{est},t'}$ denotes the estimated inertia or damping factor at time t'; t_{end} , i.e., 5s in this paper, represents the total simulation time.

Figs. 8-11 show the tracking results under both small and large Z_e . For constant and time-varying inertia tracking, it can be seen that VBUKF gets converged within 0.5 s and achieves much higher accuracy than other methods due to its adaptiveness in Q_k and R_k . Although the convergence time of D_p estimation is larger than inertia, it can get converged within 2 s. This is because inertia plays the main role in mitigating frequency deviation. However, M1 diverges in Scenarios B1-B4 since it ignores the effects of the damping factor. Although AUKF is able to track inertia quickly, it cannot estimate D_p well, which in turn deteriorates the performance on inertia tracking, see Fig. 10. This is because AUKF doesn't adaptively estimate R_k , leading to misjudgment in measurement noise, especially in time-varying inertia cases. As for M2, it can get converged in constant inertia tracking, but it requires a much longer convergence time (> 2s) and achieves a much lower accuracy. Comparing Fig. 8 with Fig. 9 or Fig. 10 with Fig.

TABLE I
ESTIMATION ERROR OF THE PROPOSED UNDER DIFFERENT
DISTURBANCES

	Inertia		Damping factor	
Scenarios	MAE _{1.5} (%)	AAE _{1.5} (%)	MAE _{1.5} (%)	AAE _{1.5} (%)
B1	3.60	1.10	1.49	0.44
B2	2.26	0.29	3.38	0.41
В3	23.25	4.11	18.15	2.97
B4	21.80	3.46	17.00	2.77
В5	1.42	0.32	2.66	0.75
В6	32.16	6.92	16.02	4.31
В7	2.47	1.00	12.76	2.32
B8	53.21	8.65	20.58	7.78

11, it can be found that the estimation accuracy of M2 is significantly affected by resistance as this is ignored in M2.

From Figs. 8-15, it illustrates that the proposed estimator tracks both inertia and D_p well in all scenarios under various disturbances. However, other methods are not robust to different scenarios. Specifically, on one hand, AUKF and M2 have much higher MAE $_t$ than VBAUKF in the constant inertia estimation scenarios, as shown in Fig. 16; on the other hand, AUKF cannot track time-varying inertia when D_p is not well estimated; M1 and M2 are not able to estimate time-varying inertia. An interesting phenomenon is that M1 can get converged when M2 and AUKF fail in estimating D_p and the proposed VBAUKF has a longer convergence time in tracking D_p , see Figs. 12-15. This may indicate that, in these cases, the damping factor has a negligible effect on frequency deviation mitigation, leading to the slow convergence of M1.

Table I demonstrates that the proposed method can estimate inertia and damping factor with high accuracy (as evidenced by the low values of $MAE_{1.5}$ and $AAE_{1.5}$) under conditions of constant inertia. In scenarios involving time-varying inertia, although the values of $MAE_{1.5}$ and $AAE_{1.5}$ are slightly higher compared to the constant inertia case, these remain at acceptable levels. As can be seen in Fig. 15, for example, the estimates exhibit small delays but closely track the inertia trends over time.

C. Performance under Various Parameters Settings

In this section, ρ is same as that in Section B, while $\vec{Z}_e = 0.1 + j0.106$.

- 1) **Performance under Different** T_a : Aiming at demonstrating the generalization of the proposed estimator, the performance under various T_a is investigated. 80% of T_a and D_p 's true values are used as their initial values. Besides, the generator located at Bus 35 is disconnected. The following scenarios are discussed:
 - Scenario C1: Constant inertia $H = \frac{1}{2}T_a = 5$ s;
 - Scenario C2: Time-varying inertia $H = \frac{1}{2}T_a = 5(\sin[2\pi(t-1)] + 2)$ s;
 - Scenario C3: Constant inertia $H = \frac{1}{2}T_a = 10$ s;

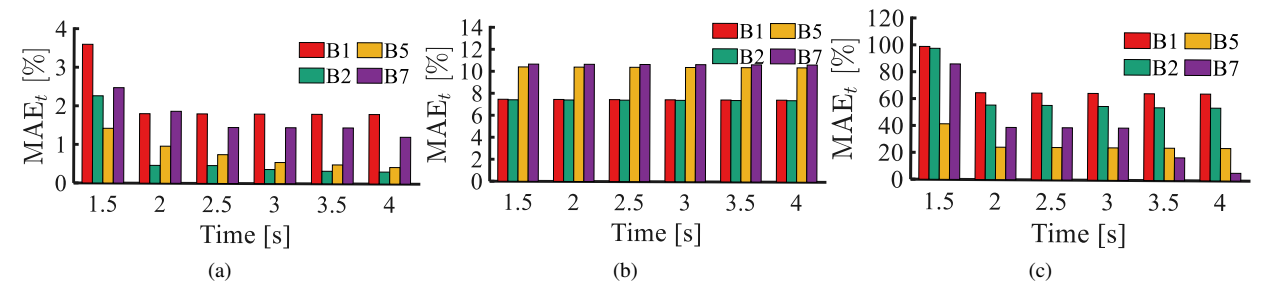


Fig. 16. Constant inertia tracking errors under multiple scenarios. (a) VBAUKF; (b) AUKF; (c) M2.

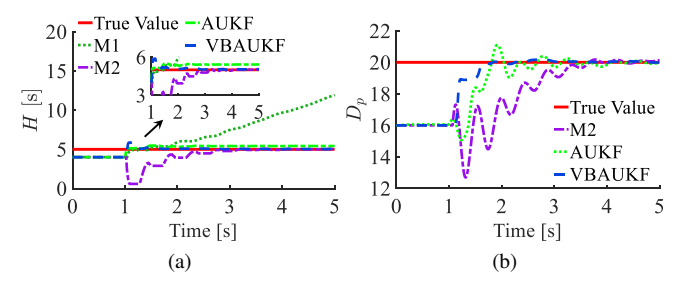


Fig. 17. Performance comparisons in Scenario C1. (a) H; (b) D_p .

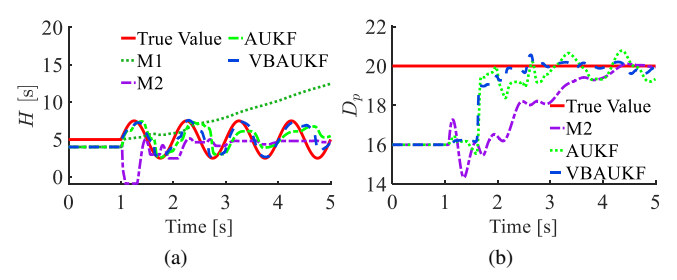


Fig. 18. Performance comparisons in Scenario C2. (a) H; (b) D_p .

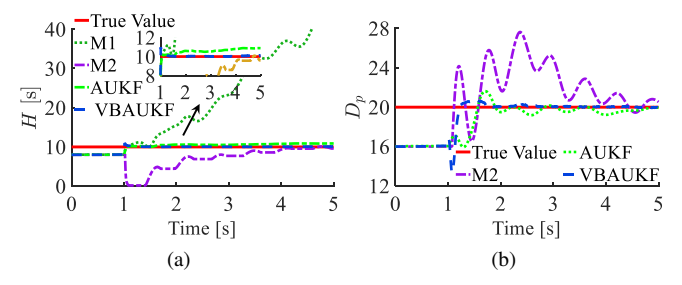


Fig. 19. Performance comparisons in Scenario C3. (a) H; (b) D_p .

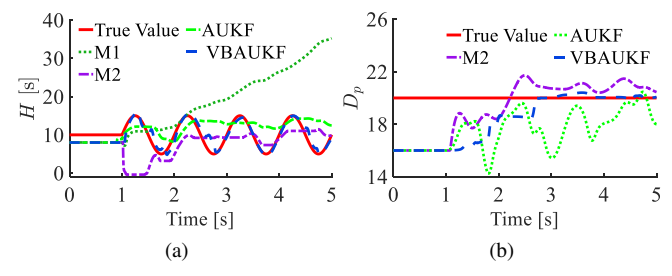


Fig. 20. Performance comparisons in Scenario C4. (a) H; (b) D_p .

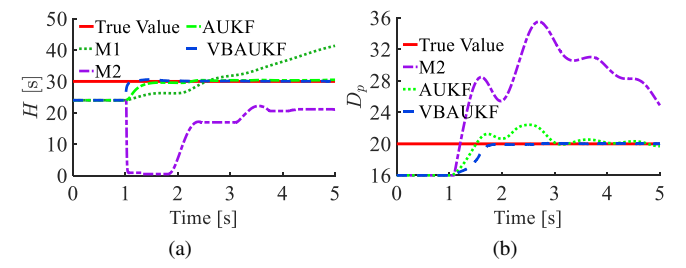


Fig. 21. Performance comparisons in Scenario C5. (a) H; (b) D_p .

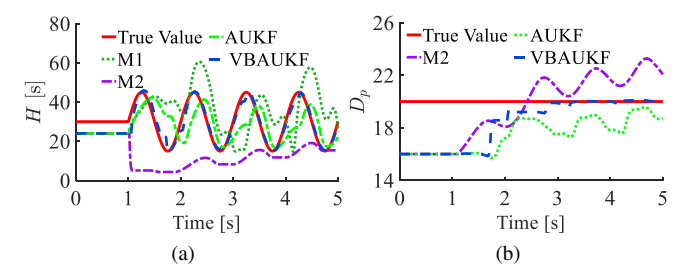


Fig. 22. Performance comparisons in Scenario C6. (a) H; (b) D_p .

- Scenario C4: Time-varying inertia $H=\frac{1}{2}T_a=10(sin[2\pi(t-1)]+2)$ s;
- Scenario C5: Constant inertia $H = \frac{1}{2}T_a = 30$ s;
- Scenario C6: Time-varying inertia $H = \frac{1}{2}T_a = 30(sin[2\pi(t-1)] + 2)$ s.

From Figs. 17-22 and Table II, it can be seen that the proposed VBAUKF has the capability of estimating constant and time-varying inertia as well as D_p under different T_a , verifying the excellent performance of the proposed estimator in tracking speed and accuracy. Due to the adaptive adjustment for Q_k as well as R_k , VBAUKF has a much better performance on estimating constant and time-varying inertia than AUKF. Besides, existing methods are not able to track timevarying virtual inertia, as shown in Figs. 18(a), 20(a) and 22(a). With the increasing of T_a , M1 tends to converge and even fluctuate following the trend of inertia. This is because larger inertia can have higher impacts on frequency mitigation, which may mask the effects of the damping factor. Consequently, the damping factor may be neglected. Since the proposed method models damping factor, different T_a doesn't have impacts on the tracking performance.

TABLE II
ESTIMATION ERROR OF THE PROPOSED UNDER VARIOUS PARAMETERS
SETTINGS

	Inertia		Damping factor	
Scenarios	MAE _{1.5} (%)	$\left. AAE_{1.5}(\%) \right $	MAE _{1.5} (%)	AAE _{1.5} (%)
C1	4.07	1.24	5.02	0.39
C2	131.91	16.94	19.26	2.04
C3	1.10	0.47	3.79	0.51
C4	76.03	11.88	18.02	3.87
C5	2.18	0.39	11.22	0.62
C6	45.22	6.08	20.75	3.16

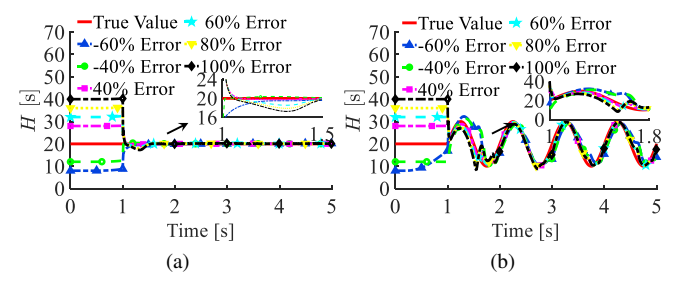


Fig. 23. Tracking results under different initial conditions (a) Constant inertia scenarios; (b) Time-varying inertia scenarios.

2) Performance under Different Initial Values of T_a : In this subsection, initial values of T_a are set as -60%, -40%, 40%, 60%, 80% and 100% errors of the true value, while the true value of T_a is 20 s. From the constant and time-varying inertia scenarios in Fig. 23, VBAUKF requires a longer time to converge when the initial values of T_a are farther away from the real value. However, the proposed method can get converged within 0.5 s even if there is a 100% error of the initial value compared with the true value.

D. Performance under Highly IBR-Penetrated Power System

The proposed method has also been validated on a highly IBR-penetrated power system. In the modified IEEE 39-bus power system, synchronous generators at Buses 30, 34, and 38 have been replaced with VSG control-based IBRs, each having the same capacity as the original synchronous generator. For these VSG control-based IBRs at Buses 30, 34, and 38, we have set T_a and D_p to 20, respectively. In the disturbance setting, the generator at Bus 35 is disconnected. We are primarily interested in estimating parameters within the VSG control-based IBRs at Bus 4, and for this purpose, we have considered both constant inertia control and time-varying control scenarios, with settings identical to those in Scenarios C3 and C4, respectively.

Figs. 24(a)-(b) illustrate the estimation results under the constant inertia control scenario, while Figs. 24(c)-(d) display the estimation results under the time-varying inertia control scenario. It is evident that in both scenarios, our proposed method accurately tracks inertia and damping factor, as shown in Table III. This success is attributed to our method's sole

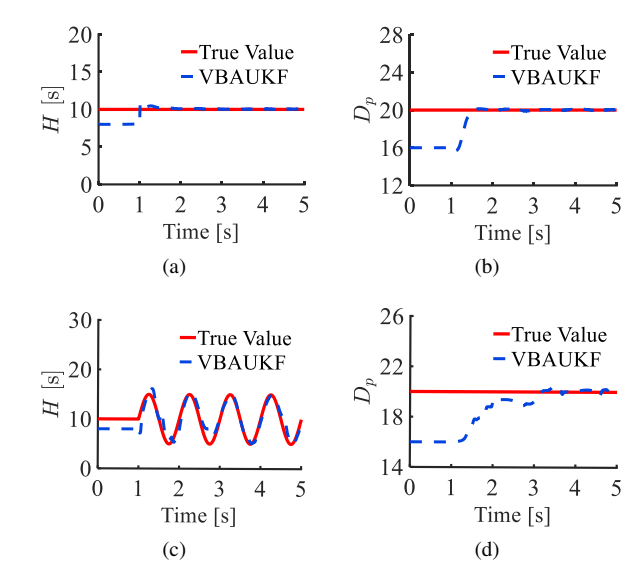


Fig. 24. Estimation result of highly IBR-penetrated power system. (a) Inertia estimation under constant inertia control; (b) Damping factor estimation under constant inertia control; (c) Inertia estimation under time-varying inertia control; (d) Damping factor estimation under time-varying inertia control.

TABLE III
ESTIMATION ERROR OF THE PROPOSED UNDER HIGHLY
IBR-PENETRATED POWER SYSTEM

	Inertia		Damping factor	
Scenarios	MAE _{1.5} (%)	AAE _{1.5} (%)	MAE _{1.5} (%)	AAE _{1.5} (%)
Constant H	2.23	0.66	1.1	0.27
Time- varying H	59.48	11.87	13.37	2.93

reliance on terminal measurements, enabling a decentralized execution manner that is not influenced by the dynamics of other generators.

E. Performance under Current Limiter

Since an inverter cannot tolerate very high currents, the current limiter is employed. In this paper, the maximum magnitude of the terminal current I_{max} is set as 1.15 p.u, as shown in Fig. 25; Line 16-21 is disconnected; $\vec{Z}_e = 0.1 + j0.106$; ρ is set as 0.9. 80% of T_a and D_p 's true values are used as their initial values. The following scenarios are investigated:

• Scenario E1: Constant inertia $H = \frac{1}{2}T_a = 40$ s;

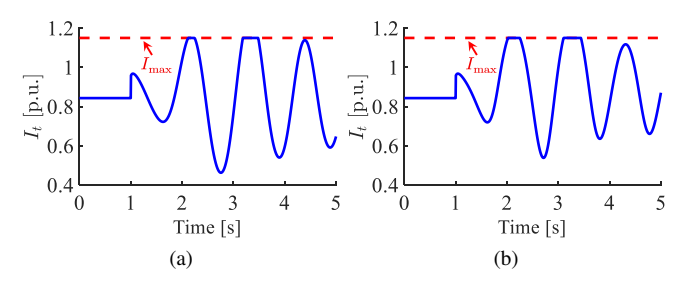


Fig. 25. Terminal currents of the inverter. (a) Scenarios E1; (b) Scenarios E2.

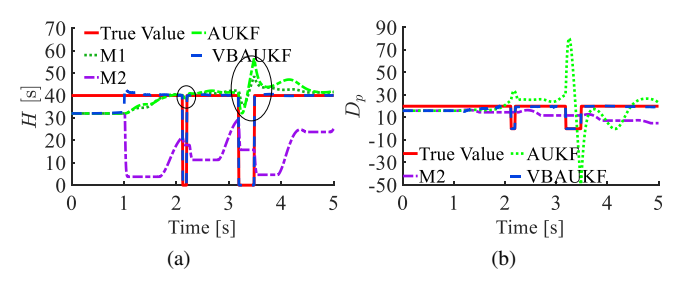


Fig. 26. Performance comparisons in Scenario E1. (a) H; (b) D_p .

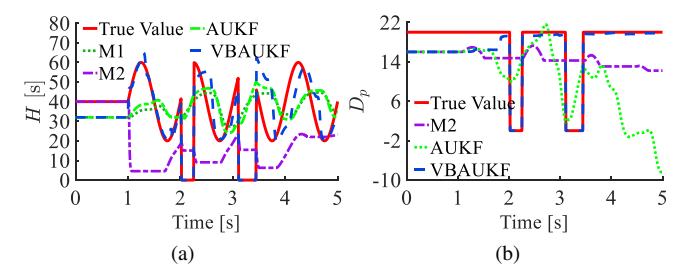


Fig. 27. Performance comparisons in Scenario E2. (a) H; (b) D_p .

• Scenario E2: Time-varying inertia $H=\frac{1}{2}T_a$ $40(sin[2\pi(t-1)]+2)$ s.

It can be observed from Fig. 25 that the current limiter stops the terminal current from increasing, leading to an inertia emulation block. As a result, these measurements may lead to discontinuities in estimation results. Fig. 26-27 show the performance of various methods under the current limiter. Because of the adaptiveness of Q_k as well as R_k , it can be seen in the constant inertia scenario that the proposed approach can mitigate effects of discontinuities caused by the current limiter. In spite of the estimation time delay in the time-varying scenario, as shown in Fig. 27, VBAUKF is still able to track the trend of inertia, although MAE_{1.5} and AAE_{1.5} are higher than scenarios without the current limiter control, as shown in Table IV. However, other methods suffer from these discontinuities, see Fig. 26.

Regarding computational efficiency, the computational load per PMU sample is quantified, as delineated in Table V. It is worth pointing out that the computing time of the proposed method for each PMU sample is much smaller than the nominal PMU scan interval of 20 ms. This demonstrates the feasibility of the introduced approach for real-time inertia and damping factor tracking.

TABLE IV
ESTIMATION ERROR OF THE PROPOSED UNDER CURRENT LIMITER

	Inertia		Damping factor	
Scenarios	MAE _{1.5} (%)	$AAE_{1.5}(\%)$	MAE _{1.5} (%)	AAE _{1.5} (%)
E1	1.54	0.46	12.50	2.50
E2	146.00	21.37	17.89	3.39

TABLE V
COMPUTATION SPEED OF THE PROPOSED METHOD PER SAMPLE

Scenarios	E1	E2
Computation Time	0.377ms	0.370ms

F. Hyperparameter Sensitivity Analysis

 ρ and β , as the forgetting factors for adjusting measurement and process noise covariance matrices, were subject to sensitivity analysis in this section. With VSG settings consistent with Scenarios E1 and E2 in the paper, we fixed β at 0.9999 and varied ρ from 0.9 to 0.95. As illustrated in Fig. 28, a lower ρ improves damping factor estimation, maintaining effective inertia estimation within the range of [0.9, 0.95]. Conversely, fixing ρ at 0.9 and varying β from 0.98 to 0.9999 shows that a higher β enhances inertia estimation, with effective damping factor estimation within [0.98, 0.9999], as shown in Fig. 29. Therefore, ρ and β can be set within [0.9, 0.95]and [0.98, 0.9999] respectively. Good results for both inertia and damping factor estimation are achieved with ρ close to 0.9 and β approaching 1. Our experience also indicates that $\beta = 0.9999$ can get fast and accurate estimation in all testing scenarios.

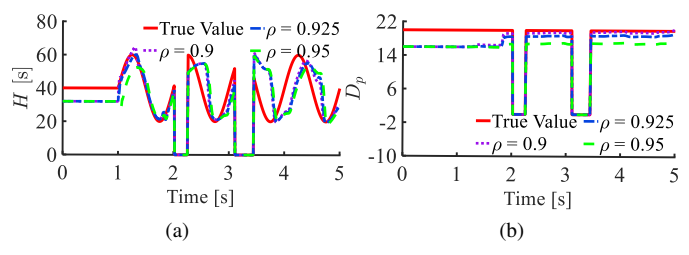


Fig. 28. Sensitivity analysis of ρ . (a) Estimation results of inertia; (b) Estimation results of damping factor.

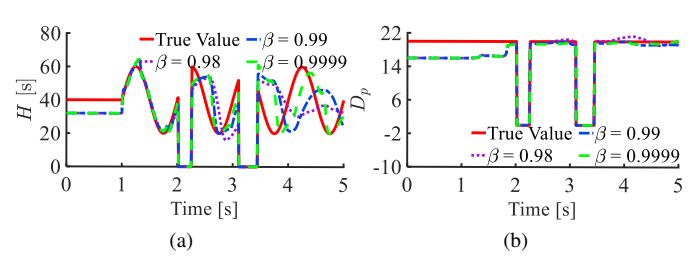


Fig. 29. Sensitivity analysis of β . (a) Estimation results of inertia; (b) Estimation results of damping factor.

G. Scalability on Large-Scale Power System

To demonstrate the scalability of our proposed method, we have conducted validation on the modified IEEE 118-bus power system, as shown in Fig. 30. Within this system, an 80-MW VSG control-based IBR is connected to Bus "Bus_119". At $t=1\,$ s, a load on Bus 74 is tripped. We have set the maximum magnitude of the terminal current $I_{\rm max}$ to be 1.15 p.u. The settings for constant inertia control and time-varying

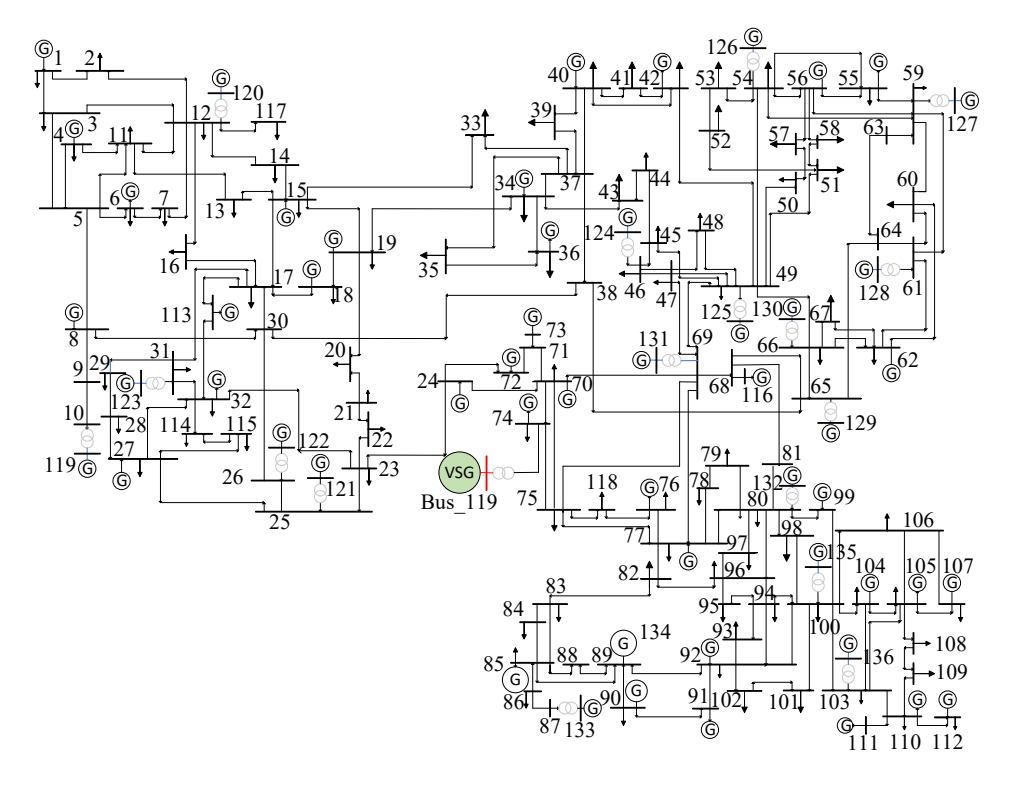


Fig. 30. The one-line diagram of modified IEEE 118-bus power system.

inertia control of VSG are identical to those in Scenarios C3 and C4, respectively.

Figs. 31(a)-(b) illustrate the estimation results under the constant inertia control scenario, while Figs. 31(c)-(d) display the estimation results under the time-varying inertia control scenario. It is evident that in both scenarios, our proposed method accurately tracks inertia and damping factor. This

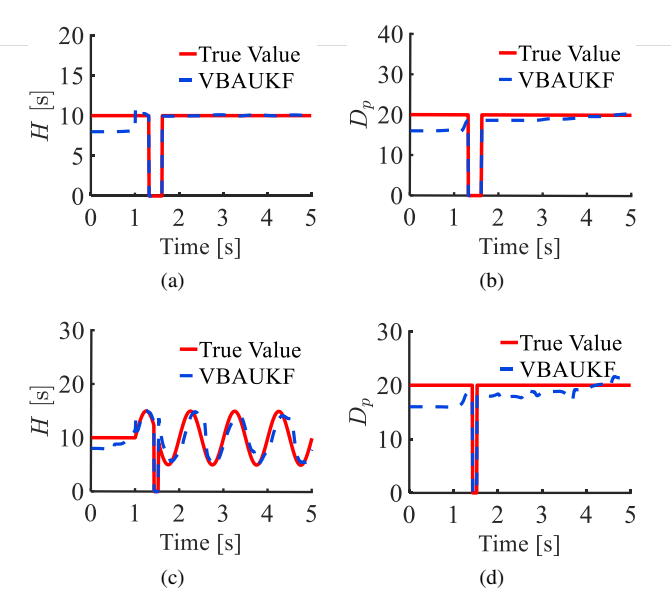


Fig. 31. Estimation result of modified IEEE 118-bus power system. (a) Inertia estimation under constant inertia control; (b) Damping factor estimation under constant inertia control; (c) Inertia estimation under time-varying inertia control; (d) Damping factor estimation under time-varying inertia control.

success stems from the fact that our method solely relies on terminal measurements, thus facilitating decentralized execution, which remains unaffected by the system size.

H. Impacts of Measurement Noise

There are unavoidable noises in PMU measurements. In line with the IEEE Standard for Synchrophasor Measurements [36], the total vector error (TVE) of measurements should be less than 1% compared with the real value. In this paper, the maximum error of measurements is considered to verify the worst scenario. The 1% TVE can be emulated via mean-zero Gaussian noise, whose standard deviation is given by [37]:

$$\sigma = \frac{\mathrm{E}[\varpi] \times 1\%}{3 \times 100} \tag{37}$$

where ϖ is the true value. Targeting at verifying the performance of the proposed estimator when measurements are corrupted by noises, the disturbance is the tripping of the generator located at Bus 35 is disconnected. \vec{Z}_e is 0.1+j0.106, while ρ is set as 0.95. 80% of T_a and D_p 's true values are used as their initial values. The following scenarios are tested:

- Scenario H1: Constant inertia $H = \frac{1}{2}T_a = 20$ s;
- Scenario H2: Time-varying inertia $H=\frac{1}{2}T_a=20(sin[2\pi(t-1)]+2)$ s.

Since M1 cannot converge in most scenarios as demonstrated in the previous sections, it is not taken as the comparison in this section. Figs. 32 and 33 show that VBAUKF can also track inertia even under the 1% TVE of measurements, though there is a time delay in estimation time-varying inertia. This is because the accurate distribution inference of \boldsymbol{R}_k and \boldsymbol{Q}_k is beneficial in filtering the noise and thus reducing the

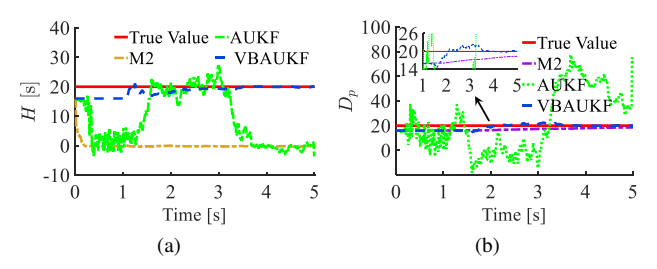


Fig. 32. Performance comparisons in Scenario H1. (a) Estimation results of inertia; (b) Estimation results of damping factor.

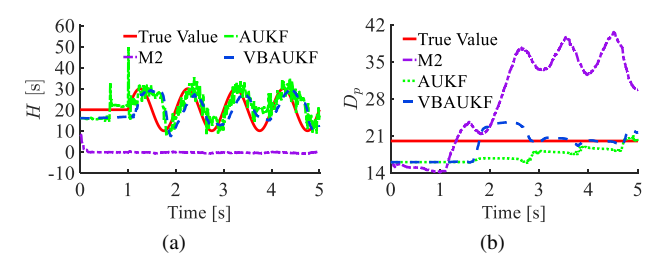


Fig. 33. Performance comparisons in Scenario H2. (a) Estimation results of inertia; (b) Estimation results of damping factor.

estimation error. However, AUKF and M2 collapse in inertia tracking due to the lack of knowledge of noise. These results illustrate that the proposed approach is more suitable for practical application.

V. CONCLUSIONS

The article develops a data-driven time-varying inertia estimation approach for VSG control-embedded IBRs by utilizing their terminal measurements. By using Thevenin equivalent to formulate the relationship between the terminal and internal voltages, the virtual frequency of IBRs is accurately estimated. Together with the estimated virtual frequency, nonlinear measurements of active and reactive power are incorporated into the Kalman filter framework, which is solved by the proposed VBUKF considering effects from the current limiter. We demonstrate that the proposed estimator performs significantly better in comparison to current state-of-art approaches. Conclusions are presented as follows:

- The proposed VBAUKF-based inertia estimator is able to infer the posterior distribution of process noise as well as measurement noise, leading to accurate and fast inertia tracking performance;
- There are unignorable effects of the damping factor on inertia tracking. As a result, it is necessary to model the damping factor into the inertia estimation framework;
- Thanks to the adaptiveness of the measurement noise covariance updating mechanism in VBUKF, the proposed estimation framework can mitigate the estimation discontinuities caused by the current limiter of IBRs, while existing state-of-art methods fail.

In this paper, we have introduced a method for estimating inertia and damping factor in fully decoupled IBRs, specifically those associated with PV or PMSG-based wind generation. Our future research endeavors will focus on extending this

method to address the complexities presented by partially coupled IBRs, such as doubly-fed induction generators (DFIGs), which exhibit more intricate inertial and damping dynamics.

REFERENCES

- B. Tan, et al., "Power system inertia estimation: Review of methods and the impacts of converter-interfaced generations,", Int. J. Electr. Power Energy Syst., vol. 134, pp. 107362, 2022.
- [2] E. Heylen, et al., "Challenges and opportunities of inertia estimation and forecasting in low-inertia power systems,", Renew. Sust. Energ., vol Rev.147, pp. 111176, 2021.
- [3] T. Inoue, et al., "Estimation of power system inertia constant and capacity of spinning-reserve support generators using measured frequency transients," *IEEE Trans. Power Syst.*, vol. 12, no. 1, pp. 136-143, Feb. 1997
- [4] P. M. Ashton, et al., "Inertia estimation of the GB power system using synchrophasor measurements," *IEEE Trans. Power Syst.*, vol. 30, no. 2, pp. 701-709, March 2015.
- [5] C. Phurailatpam, et al., "Measurement-based estimation of inertia in AC microgrids," *IEEE Trans. Sustain. Energy*, vol. 11, no. 3, pp. 1975-1984, July 2020.
- [6] B. Tan, et al., "Decentralized data-driven estimation of generator rotor speed and inertia constant based on adaptive unscented Kalman filter," Int. J. Electr. Power Energy Syst., vol. 137, pp. 107853, May. 2022.
- [7] Y. Susuki, et al., "Estimation of power system inertia using nonlinear koopman modes," in Proc. IEEE Power & Energy Soc. General Meeting, 2018, pp. 1–5.
- [8] D. Yang, et al., "Data-driven estimation of inertia for multiarea interconnected power systems using dynamic mode decomposition," *IEEE Trans. Ind. Informat.*, vol. 17, no. 4, pp. 2686-2695, April 2021.
- [9] B. Wang, et al., "An improved electromechanical oscillation-based inertia estimation method," *IEEE Trans. Power Syst.*, vol. 37, no. 3, pp. 2479-2482, May 2022.
- [10] F. Zeng, et al., "Online identification of inertia distribution in normal operating power system," *IEEE Trans. Power Syst.*, vol. 35, no. 4, pp. 3301-3304, July 2020.
- [11] A. Gorbunov, et al., "Estimation of parameters of a dynamic generator model from modal PMU measurements," *IEEE Trans. Power Syst.*, vol. 35, no. 1, pp. 53-62, Jan. 2020.
- [12] J. Liu, et al., "Online estimation of POI-level aggregated inertia considering frequency spatial correlation," IEEE Trans. Power Syst., 2022.
- [13] D. Yang, et al., "Ambient-data-driven modal-identification-based approach to estimate the inertia of an interconnected power system," IEEE Access, vol. 8, pp. 118799-118807, 2020.
- [14] K. Tuttelberg, et al., "Estimation of power system inertia from ambient wide area measurements," *IEEE Trans. Power Syst.*, vol. 33, no. 6, pp. 7249-7257, Nov. 2018.
- [15] Z. Jiang, et al., "Probing-based inertia estimation method using hybrid power plants," in 2023 IEEE Power & Energy Society General Meeting (PESGM), Orlando, FL, USA, 2023, pp. 1-5.
- [16] Y. Cui, et al., "Ambient synchrophasor measurement based system inertia estimation," in 2020 IEEE Power & Energy Society General Meeting (PESGM), Montreal, QC, Canada, 2020, pp. 1-5.
- [17] X. Cao, et al., "Switching Markov Gaussian models for dynamic power system inertia estimation," *IEEE Trans. Power Syst.*, vol. 31, no. 5, pp. 3394-3403, Sept. 2016.
- [18] J. Guo, et al., "Estimation of inertia for synchronous and non-synchronous generators based on ambient measurements," IEEE Trans. Power Syst., vol. 37, no. 5, pp. 3747-3757, Sept. 2022.
- [19] J. Guo, et al., "Online purely data-driven estimation of inertia and center-of-inertia frequency for power system with VSC-interfaced energy sources," Int. J. Electr. Power Energy Syst., vol. 137, May. 2022.
- [20] M. Liu, et al., "On-line inertia estimation for synchronous and nonsynchronous devices," *IEEE Trans. Power Syst.*, vol. 36, no. 3, pp. 2693-2701, May 2021.
- [21] B. Tan, et al., "Data-driven time-varying inertia estimation of inverter-based resources," IEEE Trans. Power Syst., 2022.
- [22] J. Chen, et al., "Adaptive virtual synchronous generator considering converter and storage Capacity limits," CSEE Journal of Power and Energy Systems, vol. 8, no. 2, pp. 580-590, March 2022.
- [23] M. Chen, et al., "Modelling, implementation, and assessment of virtual synchronous generator in power systems," *Journal of Modern Power* Systems and Clean Energy, vol. 8, no. 3, pp. 399-411, May 2020.
- [24] K.M. Cheema, "A comprehensive review of virtual synchronous generator,", Int. J. Electr. Power Energy Syst., vol. 120, pp. 106006, 2020.

- [25] J. Zhao and L. Mili. "Robust unscented Kalman filter for power system dynamic state estimation with unknown noise statistics," *IEEE Transactions on Smart Grid*, 2017, 10(2): 1215-1224.
- [26] J. Zhao and L. Mili, "A theoretical framework of robust h-infinity unscented kalman filter and its application to power system dynamic state estimation," *IEEE Transactions on Signal Processing*, vol. 67, no. 10, pp. 2734–2746, 2019.
- [27] E. A. Wan, et al., "The unscented Kalman filter for nonlinear estimation," in Proceedings of the IEEE 2000 Adaptive Systems for Signal Processing, Communications, and Control Symposium (Cat. No.00EX373), Lake Louise, AB, Canada, 2000, pp. 153-158.
- [28] P. Closas, et al., "Computational complexity reduction techniques for quadrature Kalman filters," in 2015 IEEE 6th International Workshop on Computational Advances in Multi-Sensor Adaptive Processing (CAM-SAP), Cancun, Mexico, 2015, pp. 485-488.
- [29] I. Arasaratnam, et al., "Cubature Kalman filters," IEEE Transactions on Automatic Control, vol. 54, no. 6, pp. 1254-1269, June 2009.
- [30] A. O'Hagan, et al., Kendall's Advanced theory of statistics: bayesian inference. London, U.K.: Arnold, 2004.
- [31] Y. Huang, *et al.*, "A novel adaptive Kalman filter with inaccurate process and measurement noise covariance matrices," *IEEE Trans. Automat. Control*, vol. 63, no. 2, pp. 594-601, Feb. 2018.
- [32] Appendix for "Data-driven adaptive unscented Kalman filter for time-varying inertia and damping estimation of utility-scale IBRs considering current limiter". [Online]. Available: https://www.researchgate.net/publication/365747823.
- [33] F. Zeng, et al., "Online estimation of power system inertia constant under normal operating conditions," *IEEE Access*, vol. 8, pp. 101426-101436, 2020.
- [34] M. Pai, Energy function analysis for power system stability. Springer Science & Business Media, 2012.
- [35] DIgSILENT GmbH, "DIgSILENT PowerFactory version 2022 user manual," DIgSILENT GmbH, Gomaringen, Germany, Technical Documentation, 2022.
- [36] "IEEE standard for synchrophasor measurements for power systems," IEEE Std C37.118.1-2011, pp.1-61, Dec. 2011.
- [37] R. Singh, *et al.*, "Choice of estimator for distribution system state estimation". *IET Generation, Transmission & Distribution.*, vol. 3, no. 7, pp. 666, 2009.



Bendong Tan (Student Member, IEEE) received the bachelor's and M.S. degrees in electrical engineering from Wuhan University, Wuhan, China, in 2017 and 2020, respectively. Since 2022, he has been working toward the Ph.D. degree from the University of Connecticut, Storrs, CT, USA. His research interests include low-inertia power system estimation, monitoring, and stability control.



Junbo Zhao (Senior Member, IEEE) He received the Ph.D. degree from the Bradley Department of Electrical and Computer Engineering, Virginia Tech, Blacksburg, VA, USA, in 2018. He did the summer internship with Pacific Northwest National Laboratory, Richland, WA, USA, from May 2017 to August 2017. He is currently an Associate Director for the Eversource Energy Center for Grid Modernization and Strategic Partnerships and Castleman Term Assistant Professor with the Department of Electrical and Computer Engineering, the University of Con-

necticut, Storrs, CT, USA. He is also a Research Scientist with the National Renewable Energy Laboratory, Golden, CO, USA. He was an Assistant Professor and Research Assistant Professor with Mississippi State University, Starkville, MS, USA and Virginia Tech, Blacksburg, VA, USA, from 2019 to 2021 and from 2018 to 2019, respectively. He is the Officer of multiple IEEE PES Committees and Subcommittees as well as Working Group and Task Forces, such as Renewable Systems Integration Coordinating Committee and Distribution System Analysis Subcommittee. His research interests include cyber-physical power system modeling, estimation, security, dynamics and stability, uncertainty quantification, renewable energy integration and control, and robust statistical signal processing and machine learning. He has authored and coauthored three 4 chapters and more than 200 peer-reviewed journal and conference papers, where more than 100 appear in IEEE Transactions. 7 of his papers have been listed as Highly Cited Papers. He is the Associate Editor for IEEE TRANSACTIONS ON POWER SYSTEMS, IEEE TRANS-ACTIONS ON SMART GRID, International Journal of Electrical Power & Energy Systems, the North America Regional Editor of the IET Renewable Power Generation, and Subject Editor of IET Generation, Transmission & Distribution. He has been listed as the 2020-2022 World's Top 2% Scientists released by Stanford University, Stanford, CA, USA, in both Single-Year and Career tracks. He was the receipt of the Best Paper Awards from 2020-2023 IEEE PES General Meeting (6 papers), 2022 IEEE Conference on Energy Internet and Energy System Integration, 2019 and 2022 IEEE PES ISGT Asia, 2021 IEEE Sustainable Power and Energy Conference, IEEE I&CPS Asia 2021, and 2020 Journal of Modern Power Systems and Clean Energy, 2022 Outstanding Associate Editor for IEEE TRANSACTIONS ON POWER SYSTEMS, Top 3 Associate Editor for IEEE TRANSACTIONS SMART GRID in 2020, 2020 and 2022 IEEE PES Chapter Outstanding Engineer Award, 2021 and 2022 Best Papers of IEEE TRANSACTIONS ON POWER SYSTEMS (3 papers), 2021 IEEE PES Outstanding Volunteer Award, the 2022 IEEE PES Technical Committee Working Group Recognition Award for Outstanding Technical Report, 2023 AAUP Research Excellence Award-Early Career, 2022 IEEE PES Outstanding Young Engineer Award (Society Level), and 2023 IEEE PES Technical Committee Prize Paper Award and 2023 IEEE PES Working Group Recognition Award for Outstanding Technical Report (Society Level).